



**AFRL-RX-WP-TR-2010-4190**

**COLLABORATIVE RESEARCH AND DEVELOPMENT  
(CR&D)**

**Task Order 0061: Modeling Complex Structural Geometry and  
Process Interaction**

**Bence Bartha et al.**

**Universal Technology Corporation**

**MAY 2008  
Final Report**

**Approved for public release; distribution unlimited.**

*See additional restrictions described on inside pages*

**STINFO COPY**

**AIR FORCE RESEARCH LABORATORY  
MATERIALS AND MANUFACTURING DIRECTORATE  
WRIGHT-PATTERSON AIR FORCE BASE, OH 45433-7750  
AIR FORCE MATERIEL COMMAND  
UNITED STATES AIR FORCE**

## NOTICE AND SIGNATURE PAGE

Using Government drawings, specifications, or other data included in this document for any purpose other than Government procurement does not in any way obligate the U.S. Government. The fact that the Government formulated or supplied the drawings, specifications, or other data does not license the holder or any other person or corporation; or convey any rights or permission to manufacture, use, or sell any patented invention that may relate to them.

This report was cleared for public release by the USAF 88<sup>th</sup> Air Base Wing (88 ABW) Public Affairs Office (PAO) and is available to the general public, including foreign nationals. Copies may be obtained from the Defense Technical Information Center (DTIC) (<http://www.dtic.mil>).

AFRL-RX-WP-TR-2010-4190 HAS BEEN REVIEWED AND IS APPROVED FOR PUBLICATION IN ACCORDANCE WITH THE ASSIGNED DISTRIBUTION STATEMENT.

\*//Signature//

---

MARK GROFF  
Program Manager  
Business Operations Branch  
Materials & Manufacturing Directorate

//Signature//

---

KENNETH A. FEESER  
Branch Chief  
Business Operations Branch  
Materials & Manufacturing Directorate

This report is published in the interest of scientific and technical information exchange, and its publication does not constitute the Government's approval or disapproval of its ideas or findings.

\*Disseminated copies will show “//Signature//” stamped or typed above the signature blocks.

REPORT DOCUMENTATION PAGE				Form Approved OMB No. 0704-0188	
<p>The public reporting burden for this collection of information is estimated to average 1 hour per response, including the time for reviewing instructions, searching existing data sources, gathering and maintaining the data needed, and completing and reviewing the collection of information. Send comments regarding this burden estimate or any other aspect of this collection of information, including suggestions for reducing this burden, to Department of Defense, Washington Headquarters Services, Directorate for Information Operations and Reports (0704-0188), 1215 Jefferson Davis Highway, Suite 1204, Arlington, VA 22202-4302. Respondents should be aware that notwithstanding any other provision of law, no person shall be subject to any penalty for failing to comply with a collection of information if it does not display a currently valid OMB control number. <b>PLEASE DO NOT RETURN YOUR FORM TO THE ABOVE ADDRESS.</b></p>					
1. REPORT DATE (DD-MM-YY) May 2008		2. REPORT TYPE Final		3. DATES COVERED (From - To) 11 August 2006 – 30 April 2008	
4. TITLE AND SUBTITLE COLLABORATIVE RESEARCH AND DEVELOPMENT (CR&D) Task Order 0061: Modeling Complex Structural Geometry and Process Interaction				5a. CONTRACT NUMBER F33615-03-D-5801-0061	
				5b. GRANT NUMBER	
				5c. PROGRAM ELEMENT NUMBER 62102F	
6. AUTHOR(S) Bence Bartha et al.				5d. PROJECT NUMBER 4349	
				5e. TASK NUMBER L0	
				5f. WORK UNIT NUMBER 4349L0VT	
7. PERFORMING ORGANIZATION NAME(S) AND ADDRESS(ES) Universal Technology Corporation 1270 North Fairfield Road Dayton, OH 45432-2600				8. PERFORMING ORGANIZATION REPORT NUMBER S-531-061	
9. SPONSORING/MONITORING AGENCY NAME(S) AND ADDRESS(ES) Air Force Research Laboratory Materials and Manufacturing Directorate Wright-Patterson Air Force Base, OH 45433-7750 Air Force Materiel Command United States Air Force				10. SPONSORING/MONITORING AGENCY ACRONYM(S) AFRL/RXOB	
				11. SPONSORING/MONITORING AGENCY REPORT NUMBER(S) AFRL-RX-WP-TR-2010-4190	
12. DISTRIBUTION/AVAILABILITY STATEMENT Approved for public release; distribution unlimited.					
13. SUPPLEMENTARY NOTES PAO Case Number: 88ABW 2010-1244; Clearance Date: 17 Mar 2010. Report contains color.  The U.S. Government is joint author of this work and has the right to use, modify, reproduce, release, perform, display, or disclose the work.					
14. ABSTRACT This research in support of the Air Force Research Laboratory Materials and Manufacturing Directorate was conducted at Wright-Patterson AFB, Ohio from 11 August 2006 through 30 April 2008. This task worked to help understand the effect of process variation on the behavior of complex structural components.					
15. SUBJECT TERMS nano-tailored composites, crosslinked systems					
16. SECURITY CLASSIFICATION OF:			17. LIMITATION OF ABSTRACT: SAR	18. NUMBER OF PAGES 84	19a. NAME OF RESPONSIBLE PERSON (Monitor) Mark Groff 19b. TELEPHONE NUMBER (Include Area Code) N/A
a. REPORT Unclassified	b. ABSTRACT Unclassified	c. THIS PAGE Unclassified			

## **Table of Contents**

Chapter 1	Crack Opening Displacement of Fatigue Cracks in Supersolvus IN100
Chapter 2	On the F/A-22 Full Scale Durability Test Results Regarding EIFS Values
Chapter 3	Notch Plasticity effects in Supersolvus IN100
Chapter 4	In-Situ Tensile testing of Rene 88DT at room and elevated temperatures
Chapter 5	Microstructural Conditions Contributing to Fatigue Variability in P/M Nickel-Base Superalloys
Chapter 6	Texture Separation of Alpha and Beta Phases in Duplex Microstructures
Chapter 7	Texture Separation of Alpha and Beta Phases in Duplex Microstructures
Chapter 8	Structural Modeling and Weight Optimization of Metallic Honeycomb Sandwich Thermal Protection Systems (TPS)

## **Crack Opening Displacement of Fatigue Cracks in Supersolvus IN100**

B. B. Bartha<sup>a</sup>, R. John<sup>b</sup>, M. Caton<sup>b</sup>, S. Jha<sup>a</sup>, W. J. Porter<sup>c</sup>

Universal Technology Corporation, Dayton, OH 45433

US Air Force Research Laboratory, Wright-Patterson AFB, OH 45431

University of Dayton Research Institute, Dayton, OH 45431

### **Abstract**

Fatigue crack growth tests of Supersolvus IN100 were conducted at 650C. Multiple fatigue cracks were identified during testing. The Crack Opening Displacement (COD) of each fatigue crack was investigated using Digital Image Correlation (DIC). The results were compared to Finite Element Analysis (FEA) results. While the model shows relatively good accuracy for longer fatigue cracks, the model deviates from the experimental results for the short fatigue cracks due to the effect of local microstructure and load history effects.

### **Introduction**

Fatigue variability plays a critical role in the determination of the total life in fracture critical components [ref1]. Engine Rotor Life Extension (ERLE) and Materials Damage Prognosis programs under the Air Force have examined various life limiting factors and the potential to extend the lives of in service components. Various material specific mechanisms have been found to contribute to fatigue variability. In titanium, fatigue variability was shown to be due to competing failure mechanisms [ref2]. A divergent failure mechanism has also been reported for Rene' 88DT superalloy [ref 3]. The initiation site size, location of the initiation site and the crystallographic orientation near initiation sites were shown to significantly influence the total fatigue life of Rene' 88DT. (Discuss Supersolvus IN100 fatigue data results to be published).

## Chapter 1

While previous studies have investigated the fatigue variability of nickel-base superalloys focusing on the location of crack location, the fracture mechanics of a subsequent fatigue crack also plays an important role in determining fatigue variability. The current study focuses on the fatigue crack behavior variability in supersolvus IN100 due to the local microstructure in the vicinity of a fatigue crack. The COD behavior of each fatigue crack is measured with optical microscopy combined with DIC techniques. The COD results are used to compare fatigue cracks that propagated at a different rate throughout their fatigue life, while having the same nucleation life.

Include DIC technique background in introduction or move discuss it in procedure?

### **Experimental Procedure**

A fatigue test was conducted on each specimen at a 650C temperature, a frequency of 0.33Hz, a stress ratio of 0.05 with a peak stress at 1100MPa. The fatigue experiment was interrupted at cycle numbers 1500, 2100, 2400, 2750 cycles and replicas were taken of each specimen surface at room temperature to identify the location and the size of each fatigue crack.

The specimen surface was prepared for Electron Backscatter Diffraction (EBSD) and deformation mapping after the completion of the fatigue experiment. Each sample was finish polished, and fiducial markers were placed on the surface of each specimen (Figure x1). The 5 micron fiducial marks were created with a Vickers indenter at a 50g load setting. EBSD was performed in the area of each crack to capture the grain shape and orientation in the region of interest at a 1 micron spot size resolution. Each sample was etched with nitol? solution to obtain the optimum high quality optical contrast needed for Digital Image Correlation.

Deformation mapping was performed on the fatigue cracks of interest after the completion of the fatigue test (Figure x2). A Nikon® microscope coupled to an Optronics® digital camera was used to capture 2048 by 2048 pixel image of each crack.

## Chapter 1

The specimen was loaded and unloaded at room temperature in 100MPa stress increments to 1100MPa. Images were taken of each crack for the 22 load increments.

### **Image Analysis**

Digital Image Correlation was performed on each image with ViC-2D to calculate the displacement field surrounding the crack for each load increment. The image at the 0MPa unloaded condition was used as a reference image for the displacement calculation. A subset size of 99 pixels was used for each calculation with a 5 pixels step size and cubic B-spline interpolation. The resulting displacement data was combined with the EBSD data with the aid of the fiducial markers to align the optical data with the SEM data.

The Crack Opening Displacement (COD) was measured from the displacement data obtained from the two sides of the crack mouth. The displacements calculated are relative displacements from the zero load condition, where the initial position of the crack mouth is unknown from the experimental results. Therefore, there is uncertainty in the total COD of each crack, due to the initial unknown COD condition that cannot be measured experimentally.

### **Results**

The COD measurements were compared to Linear Elastic Fracture Mechanics (LEFM) solution from Green and Sneddon (Figure x3) [ref] (Substitute Franc 3D results for Green Sneddon). The results are tabulated in Table x1. The LEFM solution under-predicted the experimental results for each crack (Figure x4). There are several reasons for the deviation of the LEFM results from the experimental results. The LEFM results do not account for the three dimensional nature of the problem relating to specimen geometry, and the local microstructure. Local plasticity effects are not included in the calculations near the crack tip and from the first shakedown cycle during the experiment. In addition the COD measurements were taken at room temperature, where the testing

## Chapter 1

was conducted at elevated temperature. None of these effects are accounted for in the LEFM calculations.

The experimental results were also compared to 3D FEA results using ABAQUS/ANSYS? Coupled with Franc-3D. The results show that the FEA predicted the COD values more accurately for the larger cracks than the smaller cracks. The COD was significantly over predicted by the 3D FEA for the short crack cases for cracks 992E and 992E. The effect of local microstructure and the effect of closure due to plasticity effects are considered to be the leading causes for the difference in the COD values for the short cracks.

### **Conclusion**

A novel optical DIC technique was used to measure the deformation and COD of fatigue cracks in supersolvus IN100. The results were compared to LEFM and 3D FEA results to show the significant difference in the COD behavior of short cracks compared to long cracks. The difference can be attributed to the effect of local grain structure and plasticity in the vicinity of fatigue cracks.

### **Acknowledgements**

This work was supported by AFOSR ... contract #

### **References**

- [ref1] Jha, S.K., Caton, M.J., Larsen, J.M., A new paradigm of fatigue variability behavior and implications for life prediction, Mat. Sci. & Eng A, 2007, 468-470, 23-32
- [ref2] Jha, S.K., Larsen, J.M., Rosenberger, A.H., The Role of Competing Mechanisms in the Fatigue-Life Variability of a Titanium and Gamma-TiAl Alloy, JOM, September 2005, 50-54



[ref3] Caton, M.J., Jha, S.K., Larsen, J.M., Rosenberger, A.H., TMS Superalloys Conference, 2004

[ref4]

## Figures and Tables

Table x1: Comparison of measured versus theoretical crack size and the number of load increments taken for each experiment.

<b>Crack</b>	<b>Crack size (<math>\mu\text{m}</math>)</b>	<b>Exp (<math>\mu\text{m}</math>)</b>	<b>GS (<math>\mu\text{m}</math>)</b>	<b>Error (%)</b>	<b>Inc (Mpa)</b>	<b>Franc 3D(<math>\mu\text{m}</math>)</b>	<b>Error (%)</b>
992A	380	1.48	1.11	25.0	100	1.48	0.0
992C	267	1.03	0.78	23.9	1100	1.04	-1.5
992D	221	0.96	0.69	28.1	1100	0.86	10.4
992E	151	0.73	0.45	39.0	100	0.59	19.2
979B	366	1.40	1.07	23.6	100	1.43	-2.1
979C	341	1.20	1.00	16.7	100	1.33	-10.8



Figure x1: Optical image of fatigue crack polished and etched for DIC and marked for combining displacement and EBSD results.

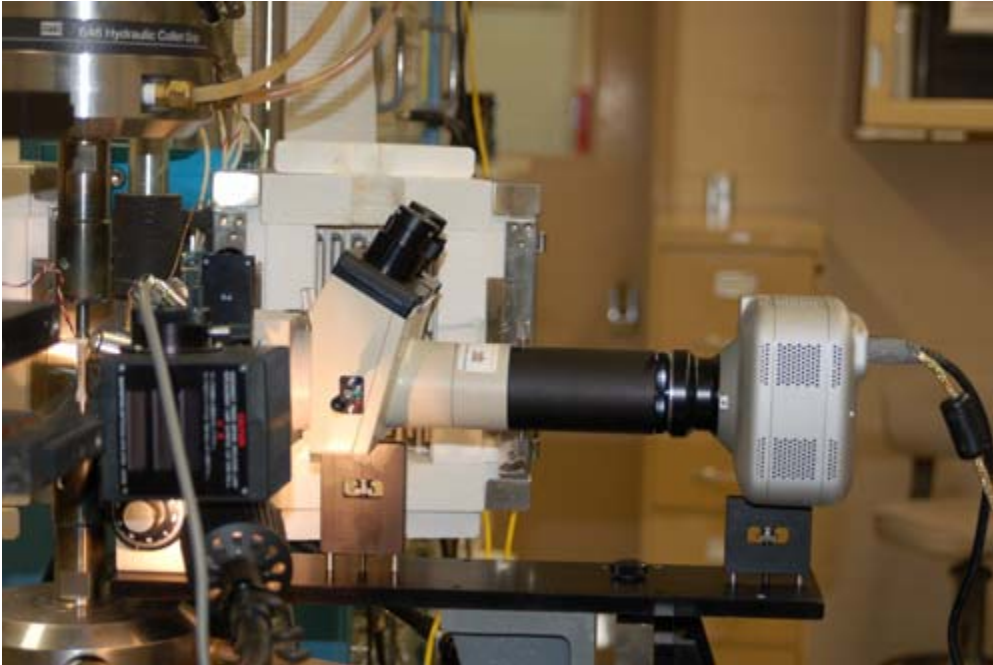
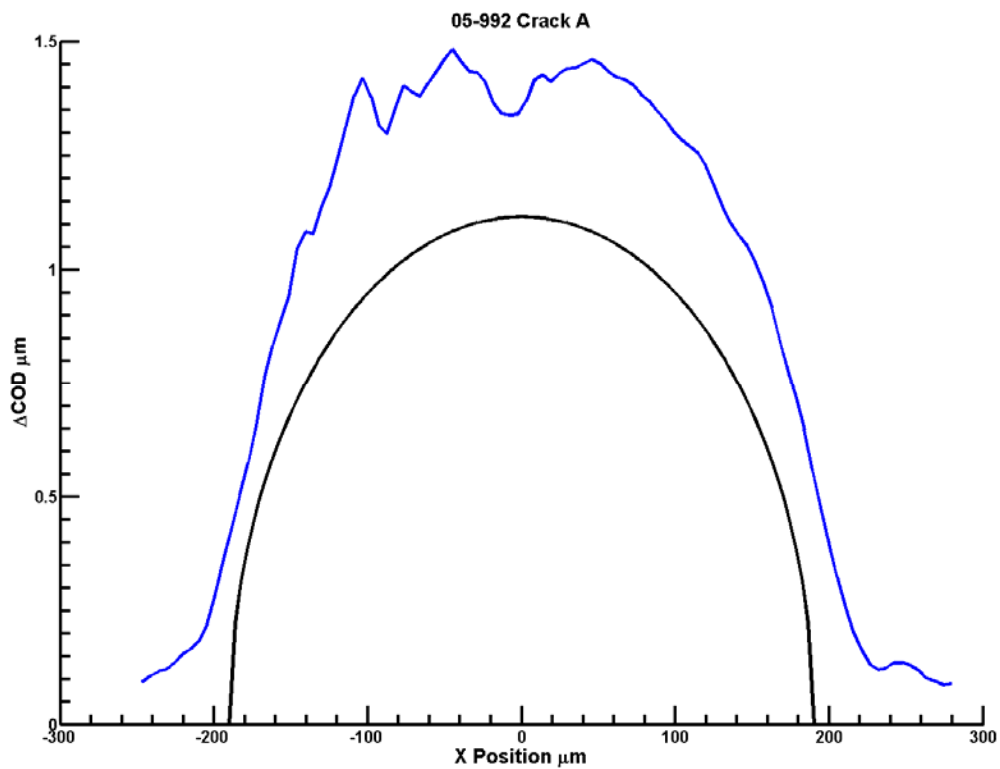
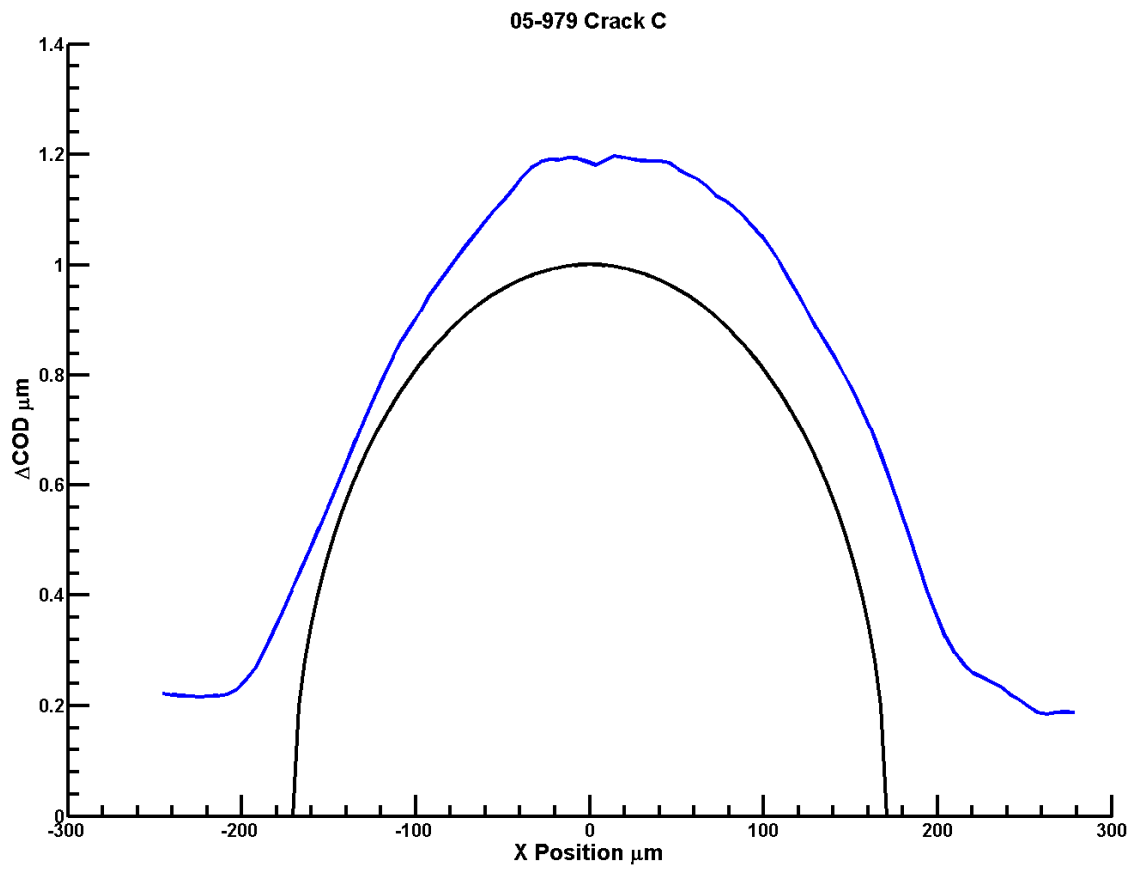
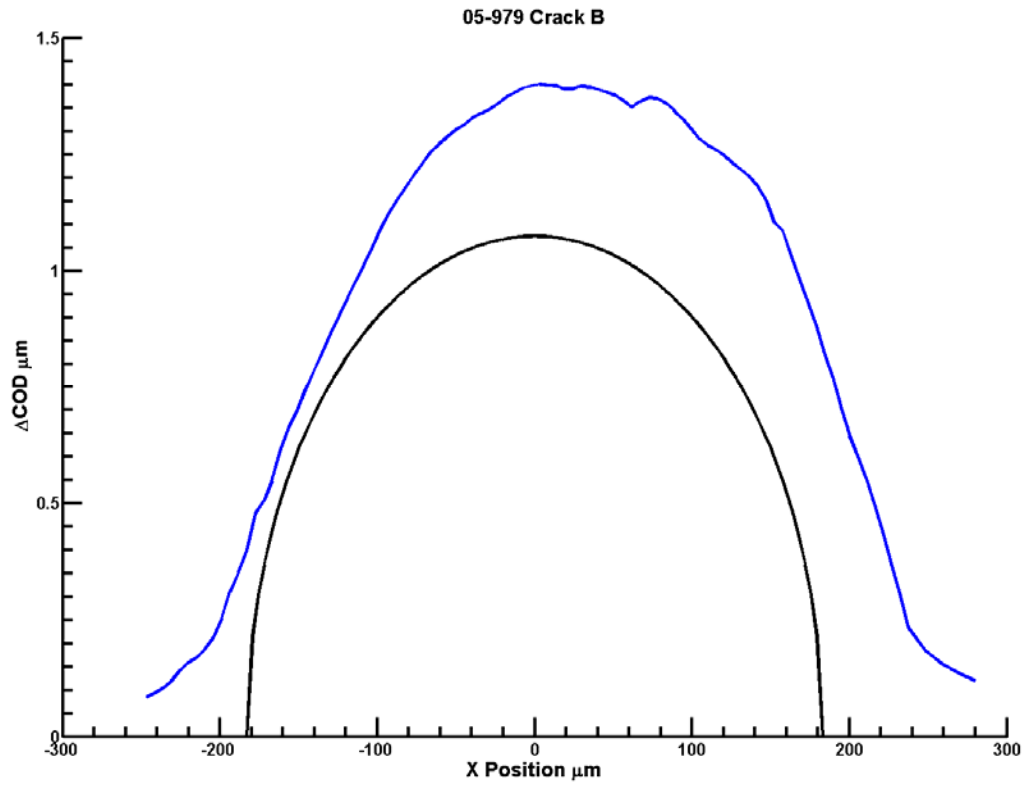


Figure x2: The experimental setup consists of an optical microscope and a digital camera coupled and mounted to a four axis stage focusing on a region of interest on the surface of a fatigue specimen.



# Chapter 1



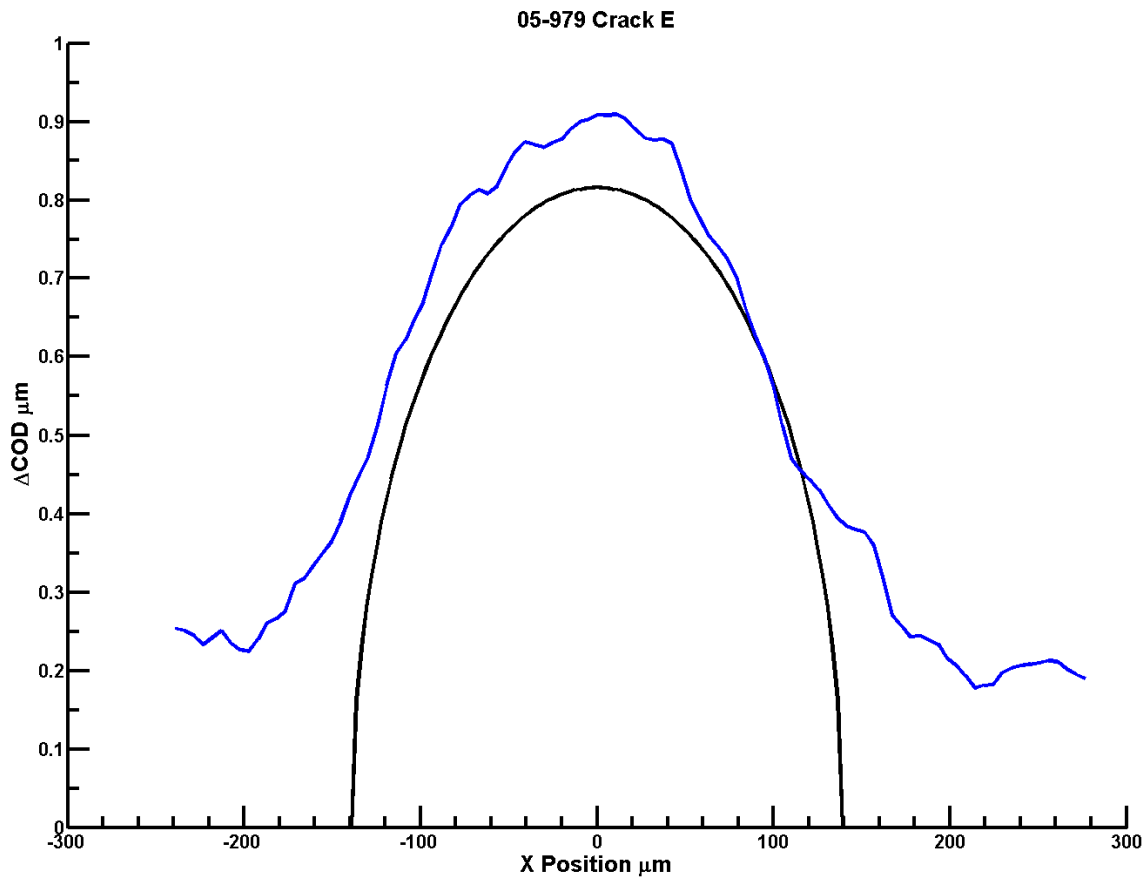
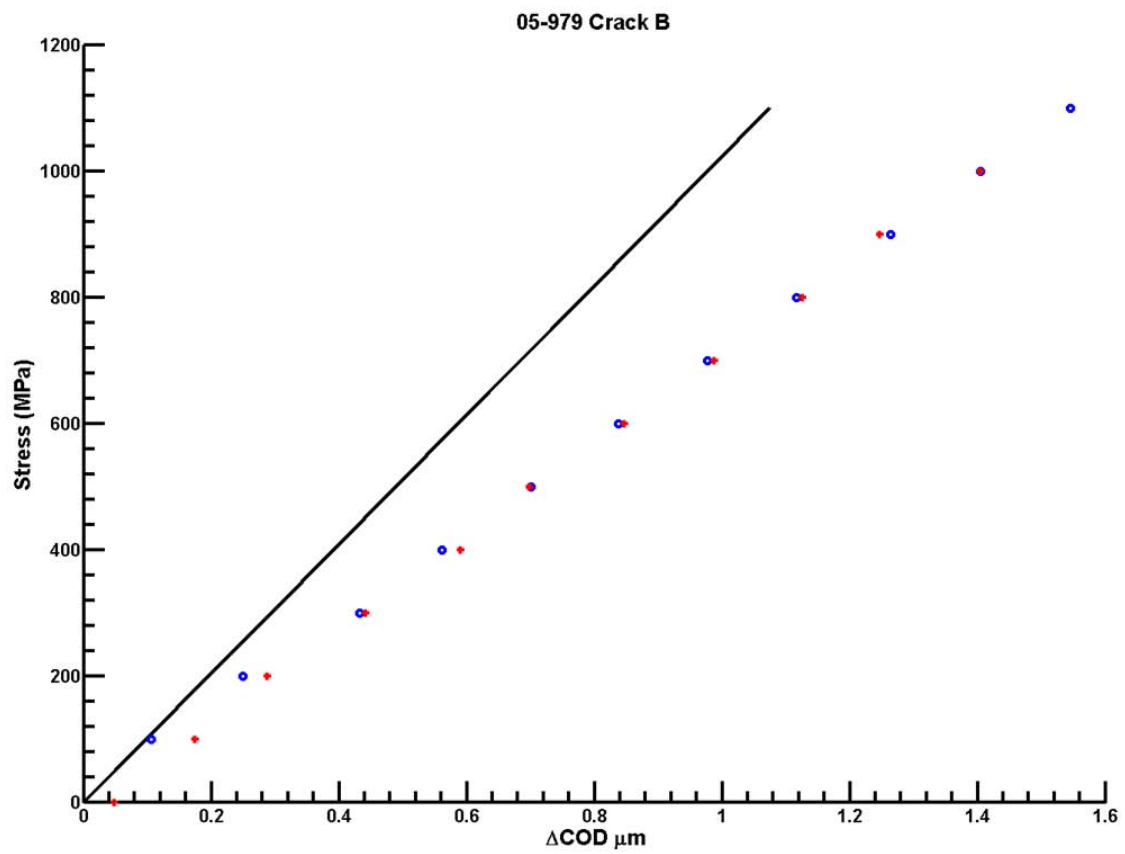
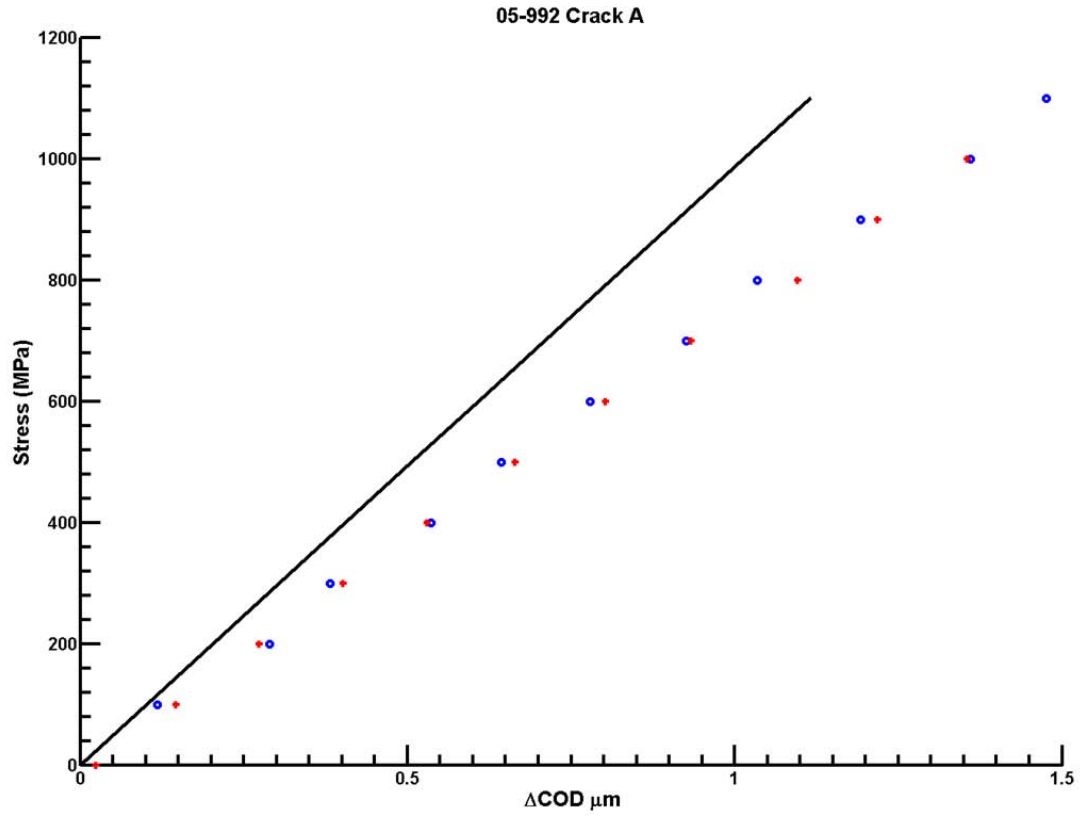


Figure x3: Relative COD is shown at 1100MPa versus 0 MPa

# Chapter 1



# Chapter 1

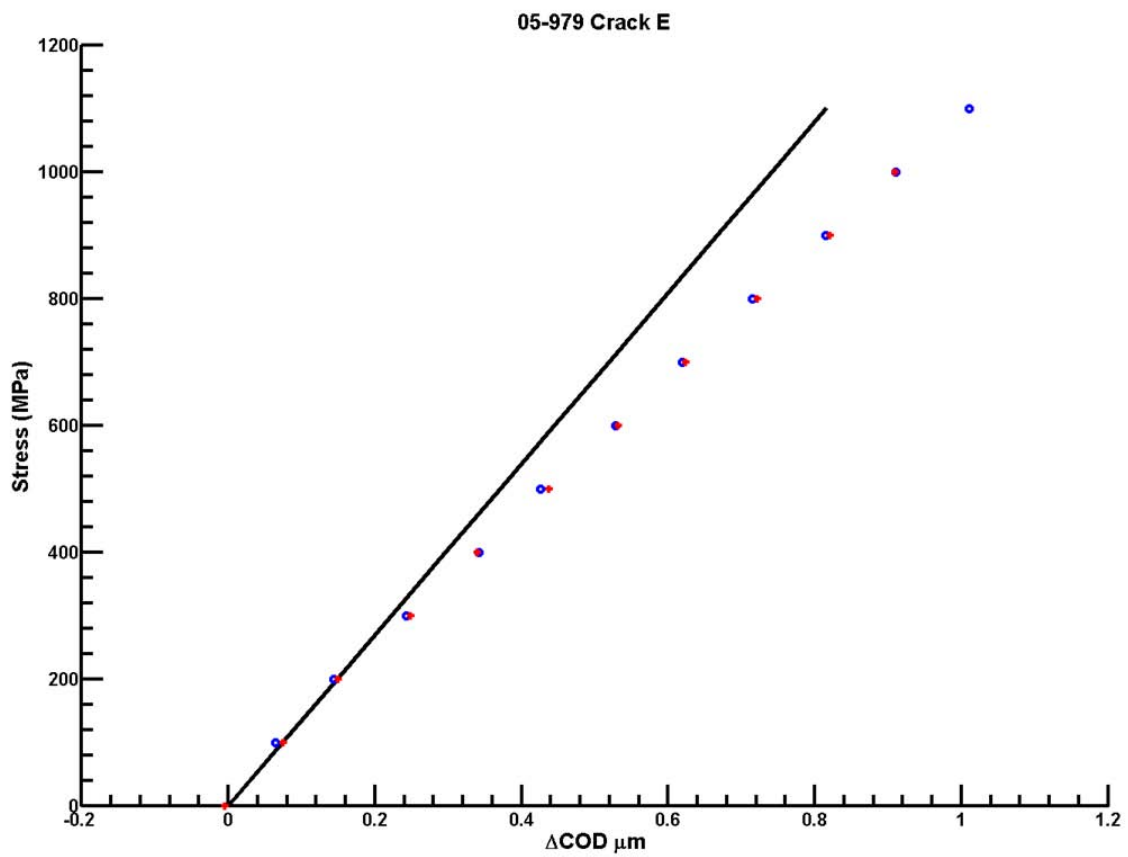
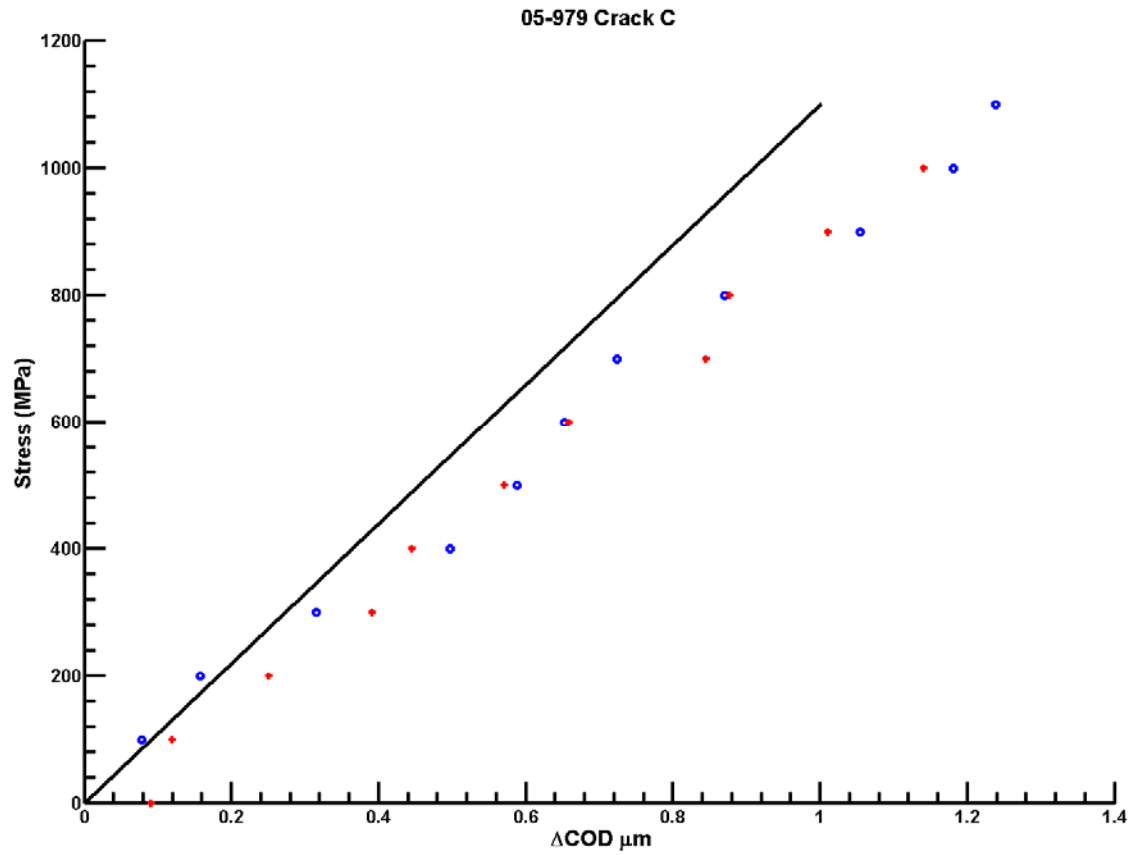
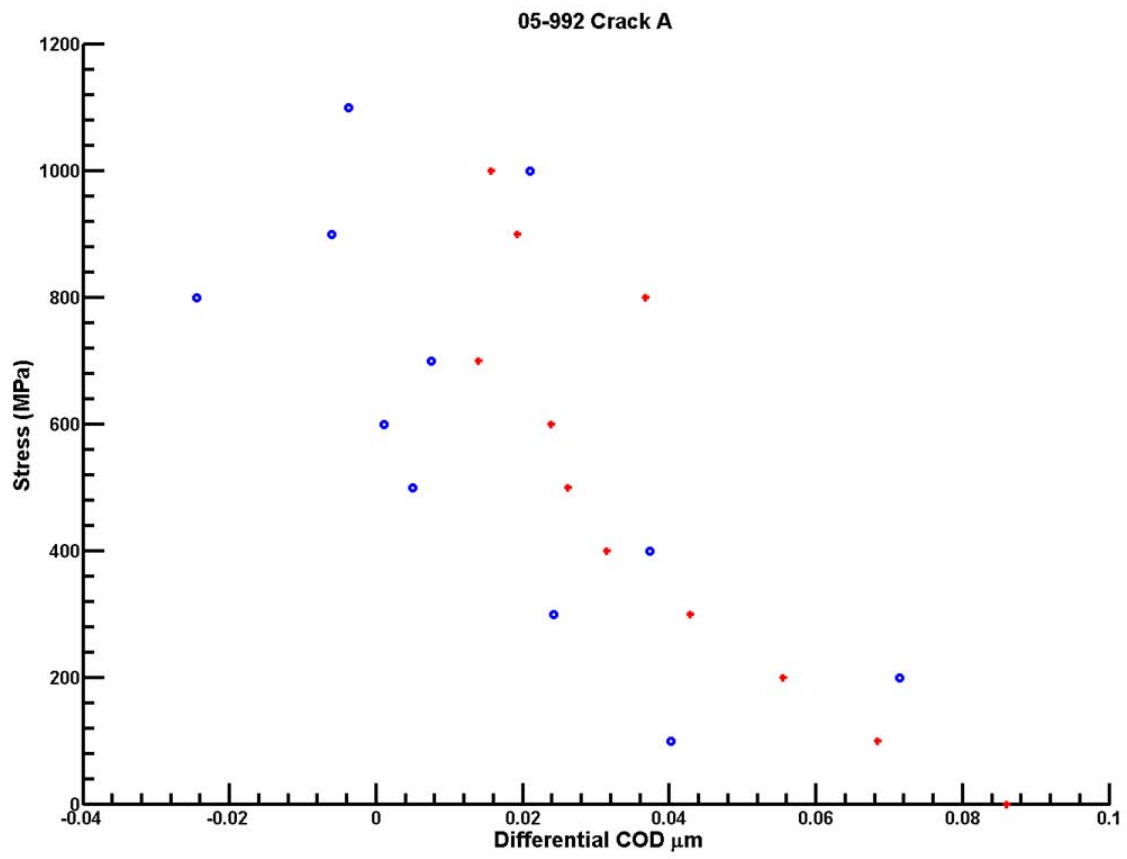
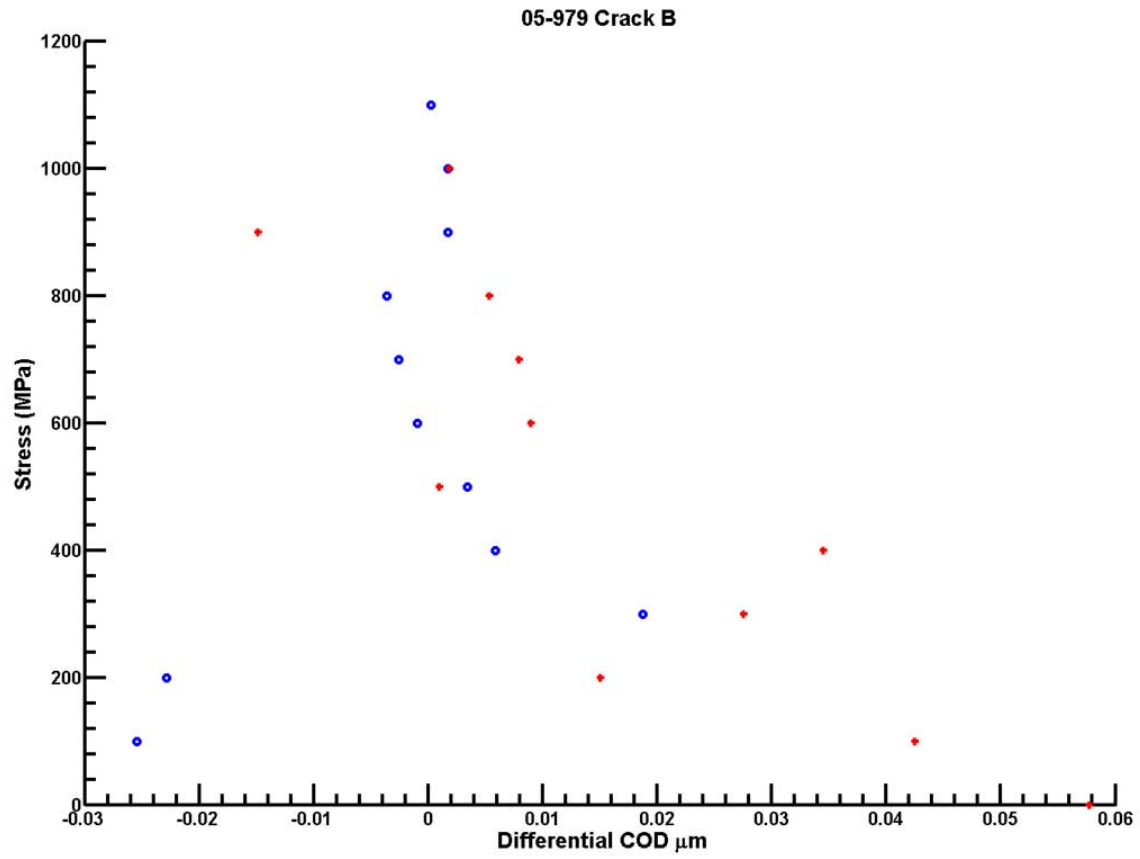


Figure x4: Peak relative crack opening displacement for loading and unloading in 100MPa increments

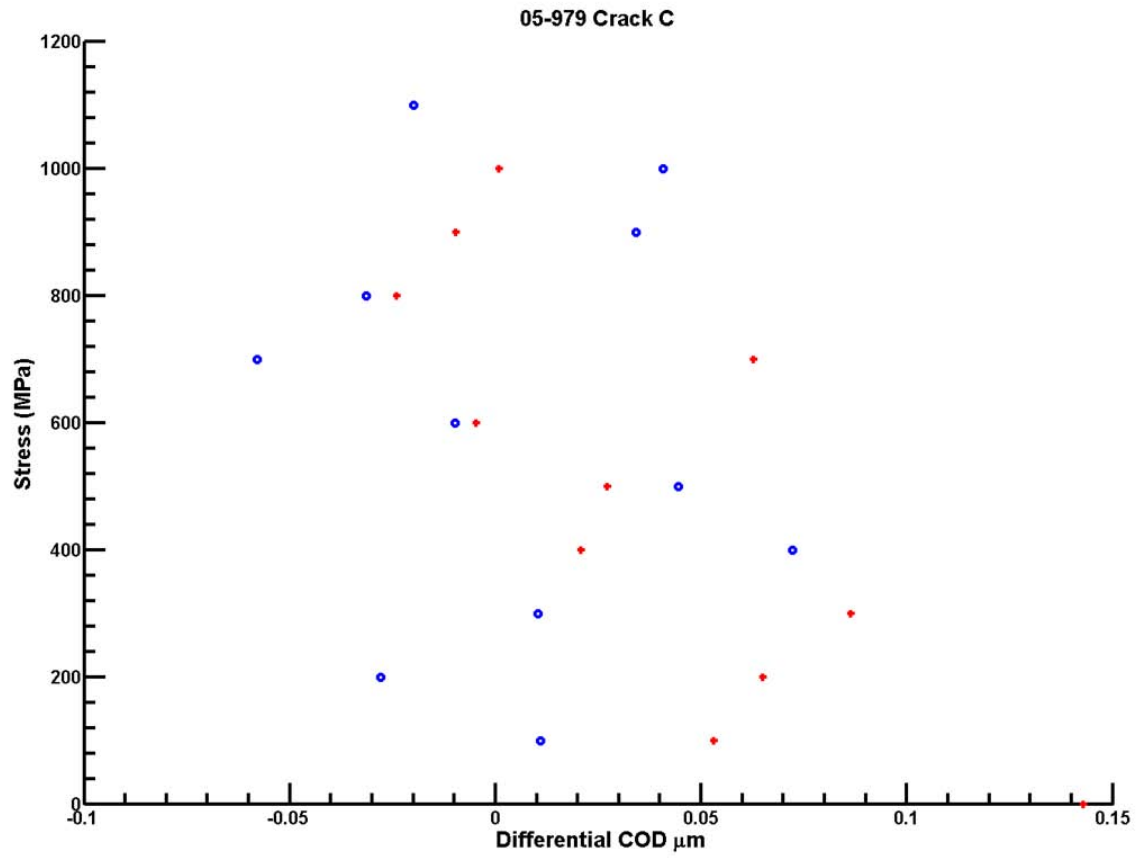


## Chapter 1





# Chapter 1



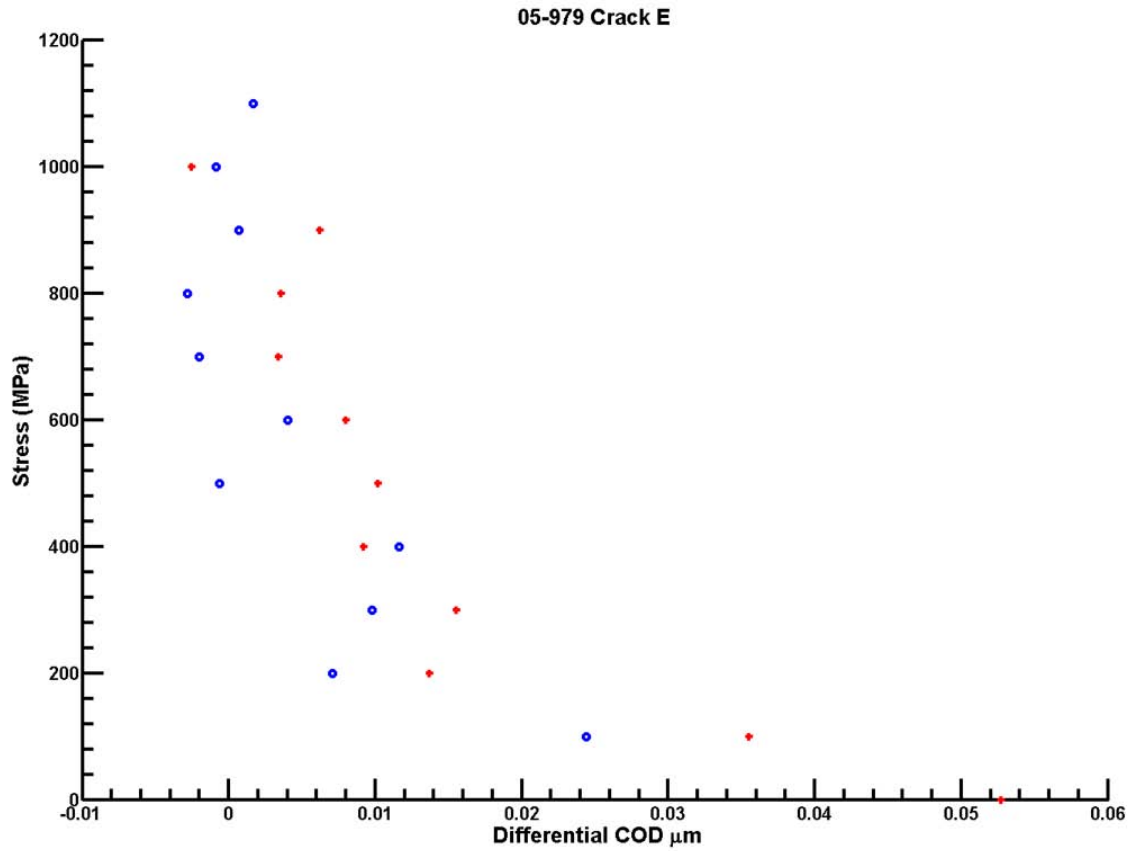
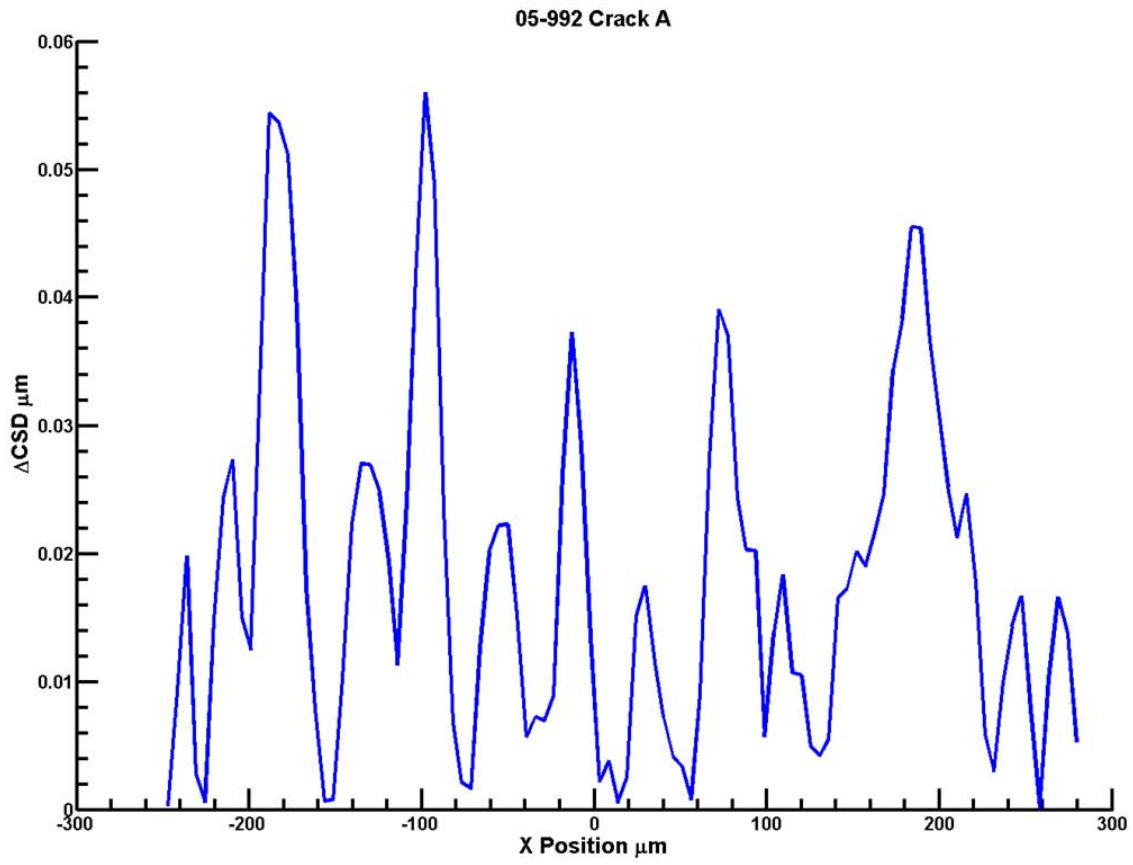
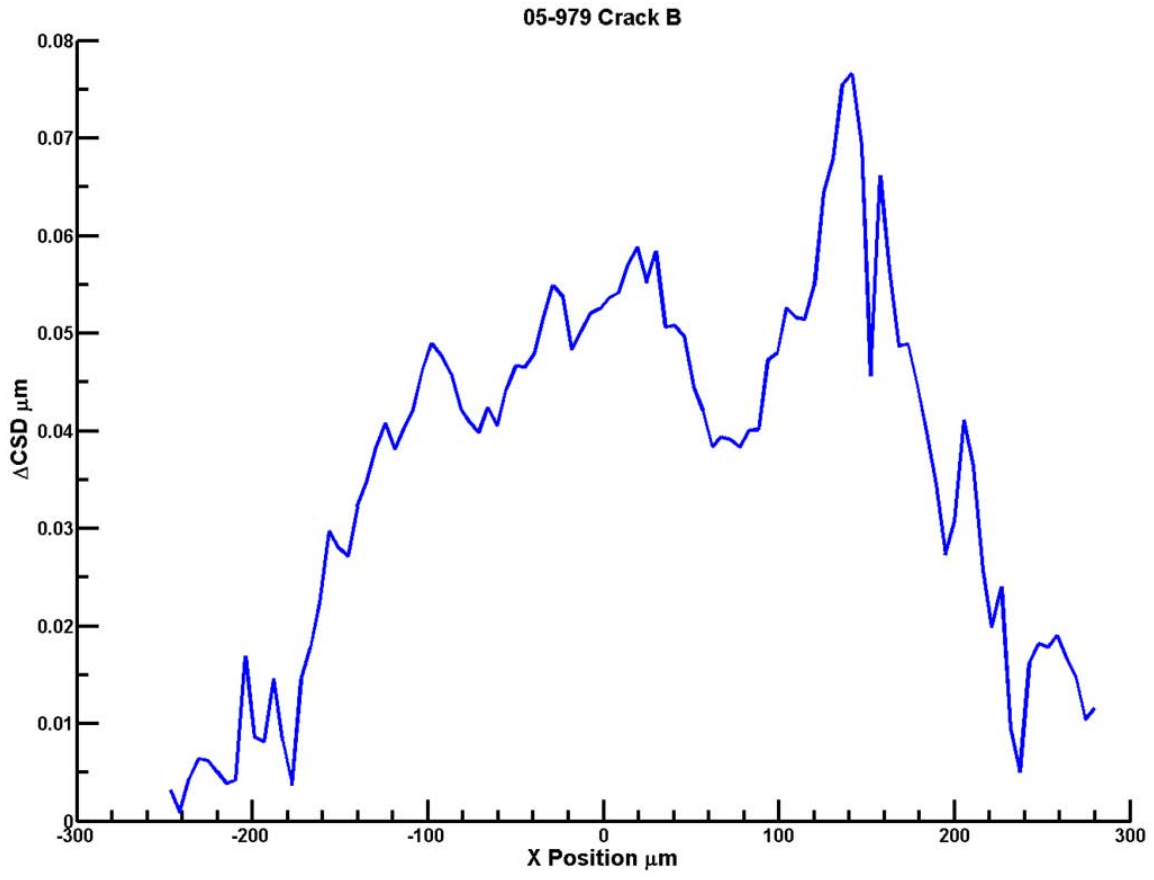
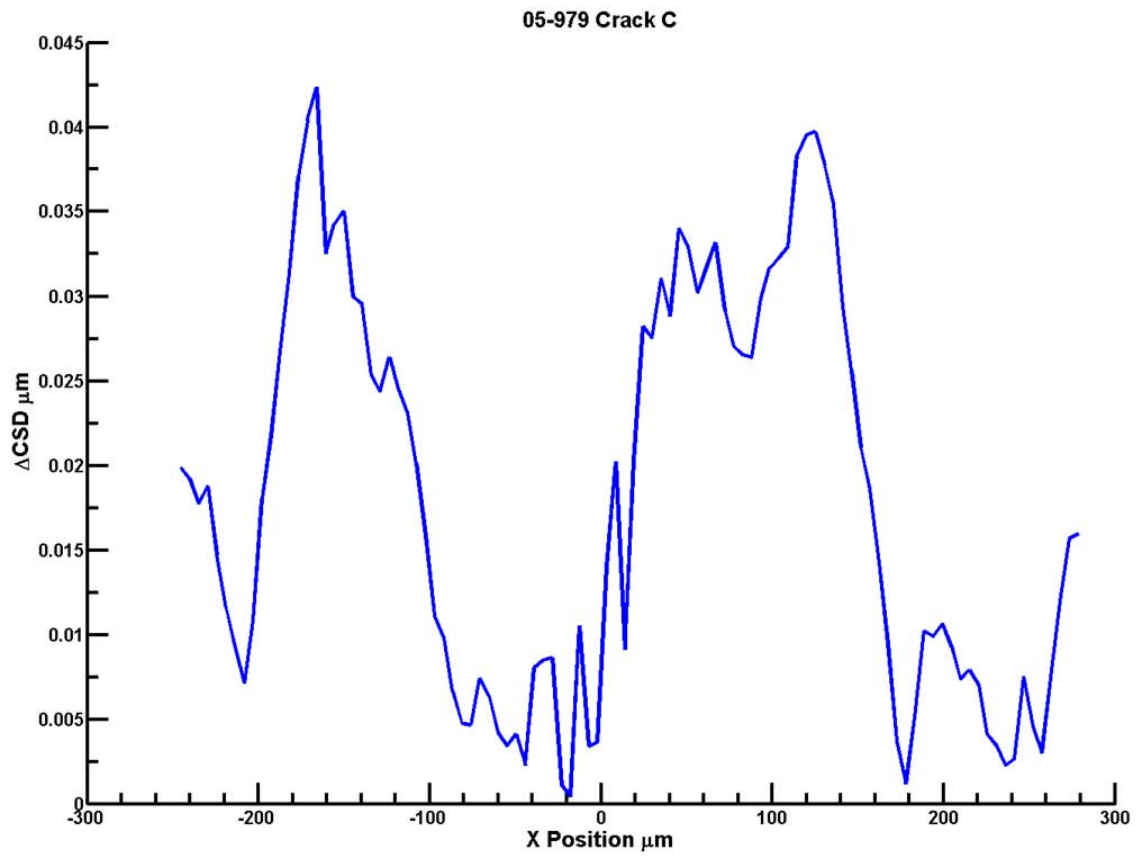


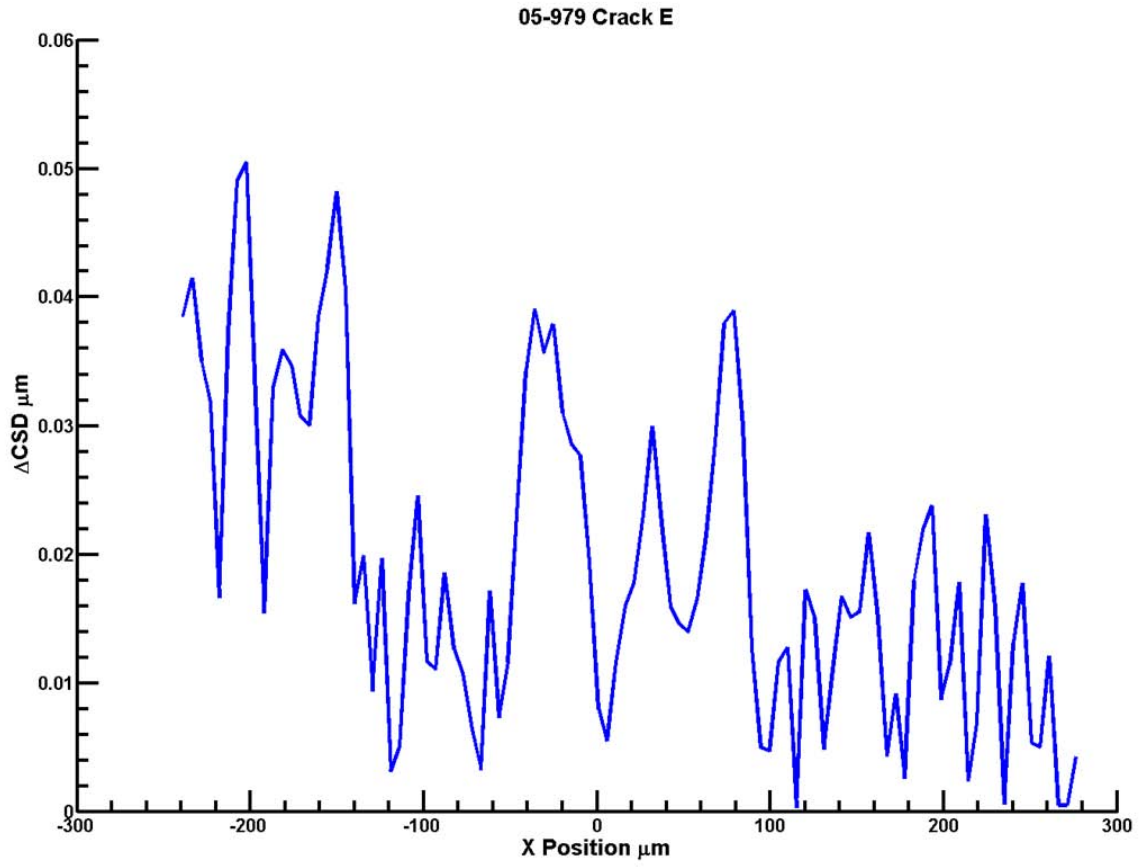
Figure x5: Differential COD is shown relative to a linear fit of the COD slope from 600MPa to 1100MPa

# Chapter 1









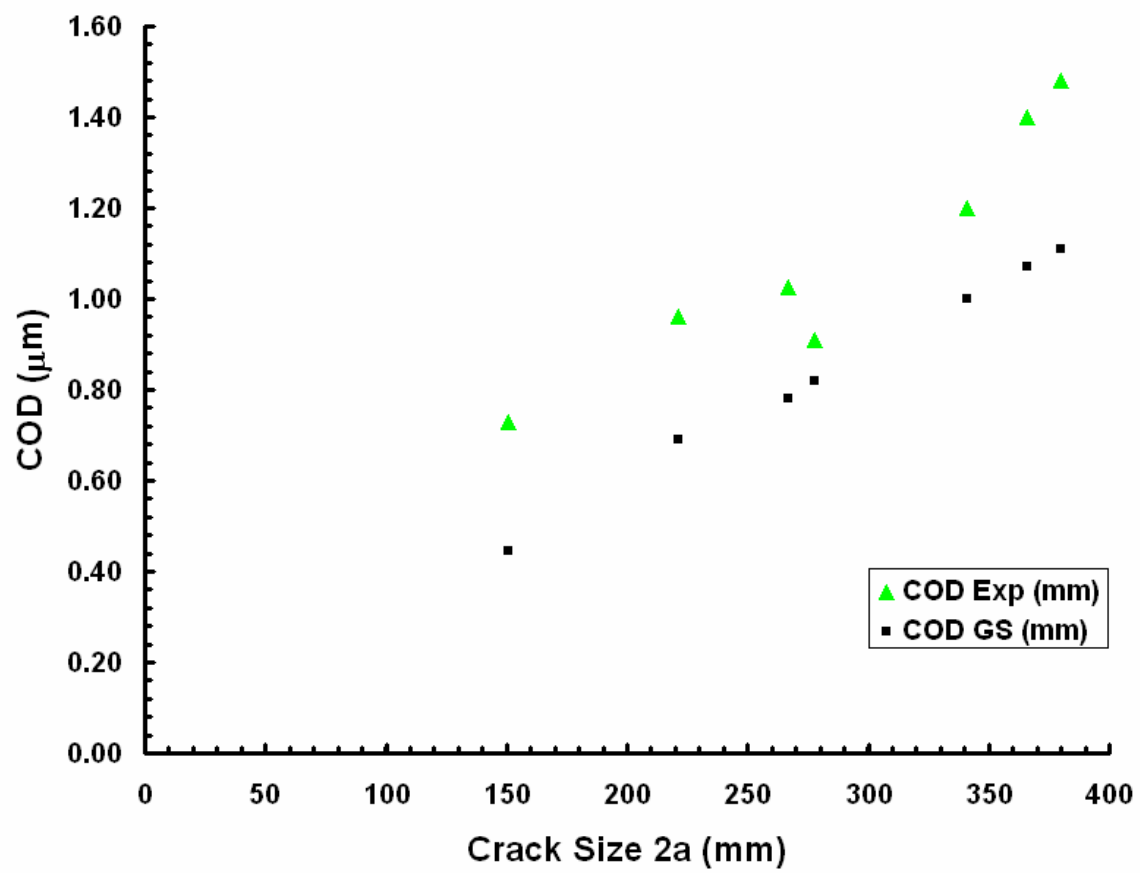


Figure x4: The COD predictions using LEFM are consistently lower than the obtained experimental values.

### On the F/A-22 Full Scale Durability Test Results Regarding EIFS Values

The calculated peak stress (99-155ksi) in the analysis of the cracks in TAR 45 are near, or over the yield stress (120ksi) for the material. The shakedown during the initial plastic deformation, and strain hardening due to these stresses affects not only the EIFS, but also the initiation life and the subsequent crack growth properties of the material. The test program will include both smooth bar and notch fatigue tests to investigate such effects. 10 uniaxial smooth bar and 10 notch fatigue tests (3 grain sizes ranging from 0.015 up to 0.05 and 3 repeats - 1 test for tuning of replication procedures) will investigate the experimental EIFS, possible grain boundary and size effects, as well as initiation and crack growth properties. The loading range and notch radius will be chosen to produce stress magnitudes and gradients near the values predicted by the durability testing. Acetate replication will monitor the crack initiation and size at various points during fatigue life. The plastic zone size will be determined with 2-D strain mapping techniques.

The overview of Crack 2 in TAR 45 mentions that the determination of the initiation is obtained from the local stress distribution near a notch. *“Calculate initiation times by multiplying reference stress values by the Boeing shallow gradient (SSG) factor before determining initiation life. The stress gradient is defined as the delta stress in the first 0.05 in of distance from the peak stress divided by 0.05.”* It is ambiguous whether the SSG includes previous S/N or experimental data. It is also unclear how the spectrum loading is included in the initiation life calculations. Potentially, a comparison between the initiation data generated from the above fatigue tests and the initiation life analysis will enhance the accuracy of the initiation life prediction.

The peak stress near the location of the cracks is predicted by a coarse FE mesh that brings uncertainty to the accuracy the peak surface, and subsurface stress distribution. Unaccounted shape factor effects in some of the redesigned components, as mentioned in TAR 45, further decrease the accuracy of the FE model. *“The lower lug fillet was changed to remove most of the stress concentration that caused crack 2 at A/C4008. There is no detailed solid element FEM of this particular configuration and so the correlated margins and lives quoted are taken from BA312/Crack 1 to be conservative.”* Higher order elements may not be sufficient to obtain the stress distribution accurately for notches that have high peak stress, and sharp stress gradients with respect to the overall element size. A convergence study of the peak stress and the stress distribution is necessary to determine the degree of mesh refinement needed in these regions. Sub-models that include the hotspots are necessary for verification. The accurate subsurface stress distributions will enhance the precision of both the initiation and the crack growth analysis.



## **Notch Plasticity effects in Supersolvus IN100**

B. B. Bartha<sup>a</sup>, R. John<sup>b</sup>, M. Caton<sup>b</sup>, S. Jha<sup>a</sup>, W. J. Porter<sup>c</sup>

Universal Technology Corporation, Dayton, OH 45433

US Air Force Research Laboratory, Wright-Patterson AFB, OH 45431

University of Dayton Research Institute, Dayton, OH 45431

### **Abstract**

A tensile test of Supersolvus IN100 was conducted at room temperature. Multiple notches were placed on the surface of the specimen using a Focused Ion Beam (FIB). Deformation mapping was conducted on each notch during the tensile tests. Digital Image Correlation (DIC) was performed on the obtained images to obtain the plasticity near each notch area. The strain results were compared to the grain orientation data.

### **Introduction**

Fatigue variability plays a critical role in the determination of the total life in fracture critical components [ref1]. Engine Rotor Life Extension (ERLE) and Materials Damage Prognosis programs under the Air Force have examined various life limiting factors and the potential to extend the lives of in service components. Various material specific mechanisms have been found to contribute to fatigue variability. In titanium, fatigue variability was shown to be due to competing failure mechanisms [ref2]. A divergent failure mechanism has also been reported for Rene' 88DT superalloy [ref 3]. The initiation site size, location of the initiation site and the crystallographic orientation near initiation sites were shown to significantly influence the total fatigue life of Rene' 88DT. (Discuss Supersolvus IN100 fatigue data results to be published).

While previous studies have investigated the fatigue variability of nickel-base superalloys focusing on the location of crack location, the fracture mechanics of a subsequent fatigue crack also plays an important role in determining fatigue variability. The current study

focuses on the crystal plasticity behavior in supersolvus IN100 due to the local microstructure in the vicinity of fatigue notches. The crystal plasticity behavior of each FIB notch is measured with optical microscopy combined with DIC techniques. The results are used to compare the FIB notches to the local grain structure and orientation.

### **Experimental Procedure**

A tensile test was conducted on a specimen at a room temperature to a peak stress at 1100MPa.

Before the tensile test, the specimen surface was prepared for FIB notch placement, and Electron Backscatter Diffraction (EBSD). Each sample was finish polished, and seven 40  $\mu\text{m}$  FIB notches were placed 150 mm apart on the surface of each specimen. EBSD was performed in the area of each FIB notch to capture the grain shape and orientation in the region of interest at a 1 micron spot size resolution. The sample was etched with nitol solution to obtain the optimum high quality optical contrast needed for DIC

Deformation mapping was performed on the FIB notches after the completion of the fatigue test (Figure x2). A Nikon® microscope coupled to an Optronics® digital camera was used to capture 2048 by 2048 pixel image of each crack. The specimen was loaded and unloaded at room temperature in 100MPa stress increments to 1100MPa. Images were taken of each crack for the 22 load increments.

### **Image Analysis**

Digital Image Correlation was performed on each image with ViC-2D to calculate the displacement field surrounding the crack for each load increment. The image at the 0MPa unloaded condition was used as a reference image for the displacement calculation. A subset size of 99 pixels was used for each calculation with a 5 pixels step size and cubic B-spline interpolation. The resulting displacement data was compared to the EBSD data.

### **Results**

Figures 1-14 show the local strain behavior of supersolvus IN100 around seven FIB notches. While the nominal strain behavior of each of the seven areas of interest were similar, there were variations in the local strain behavior due to the microstructure near each FIB notch. The highest local strain results may be an indicator as to which FIB notch will cause a crack to initiate first. Further investigation and fatigue testing is necessary in this case to obtain the fatigue crack growth results, and to compare the final fatigue data to the initial plastic behavior of the seven regions for the first cycle tensile test.

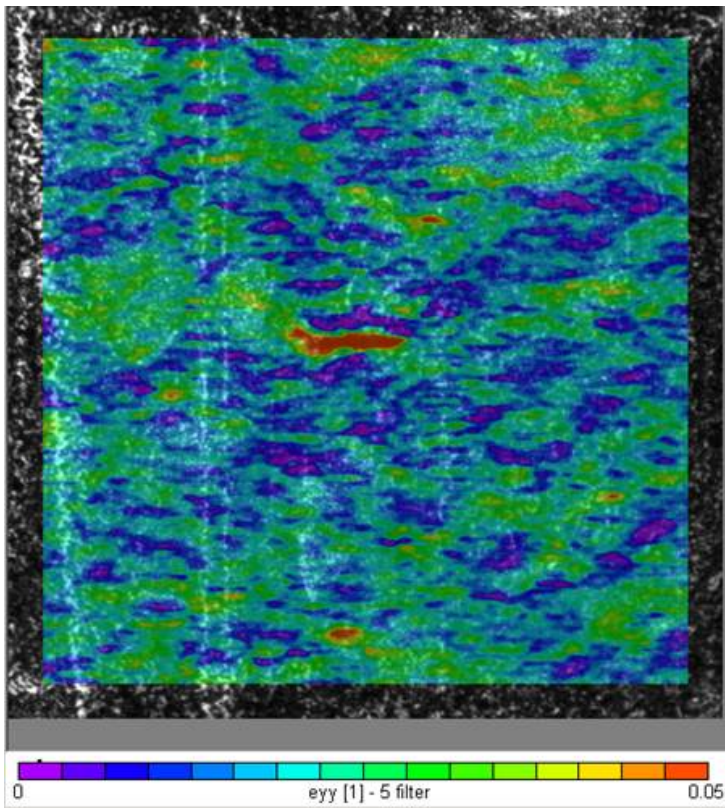


Figure 1: Notch 1 strain distribution at 900MPa

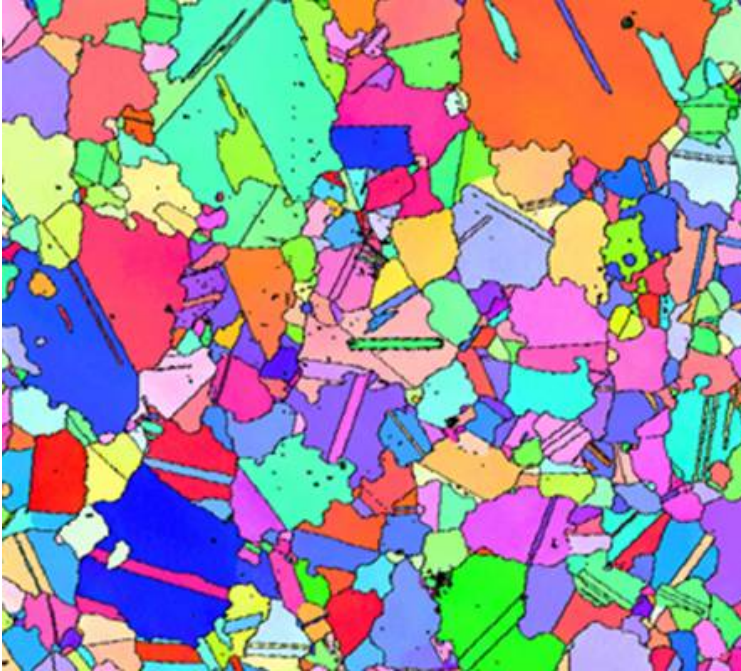


Figure 2: Notch 1 inverse pole figure of local microstructure.

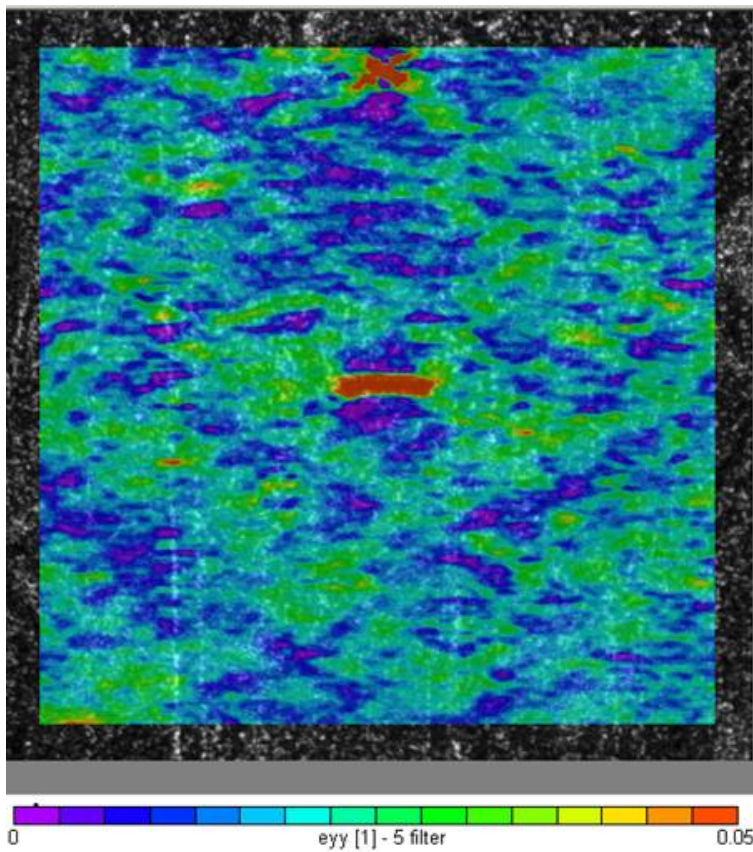


Figure 3: Notch 2 strain distribution at 900MPa



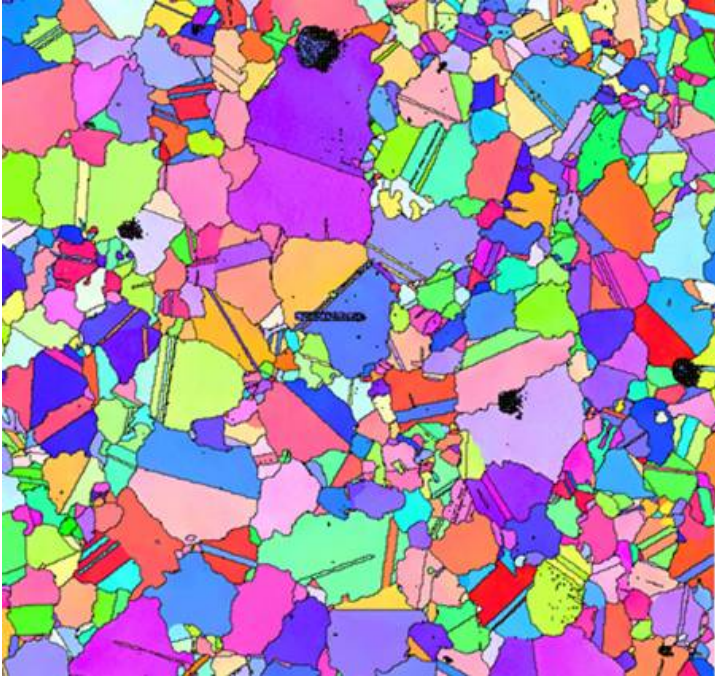


Figure 4: Notch 2 inverse pole figure of local microstructure.

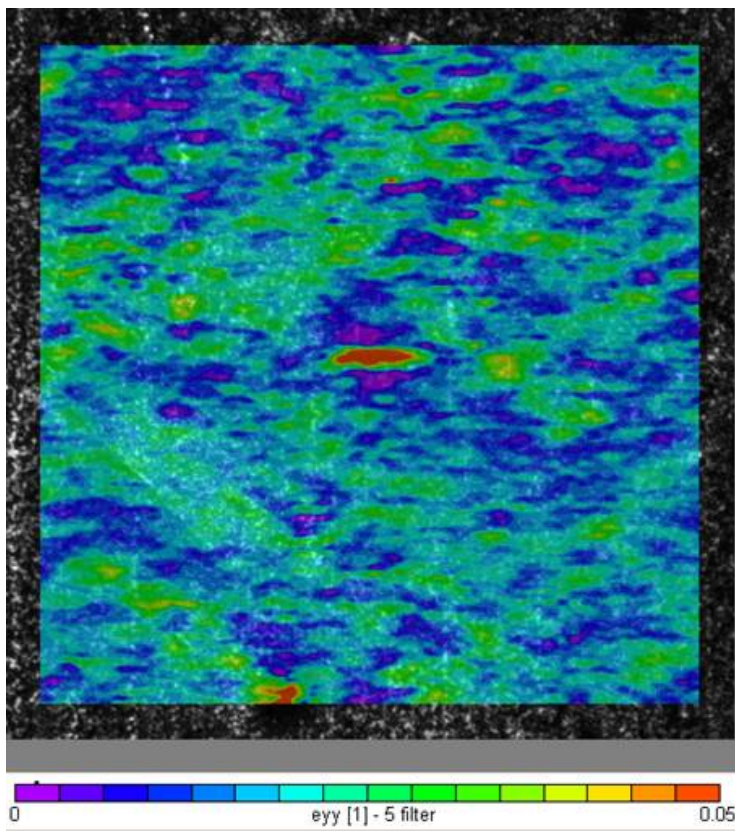


Figure 5: Notch 3 strain distribution at 900MPa

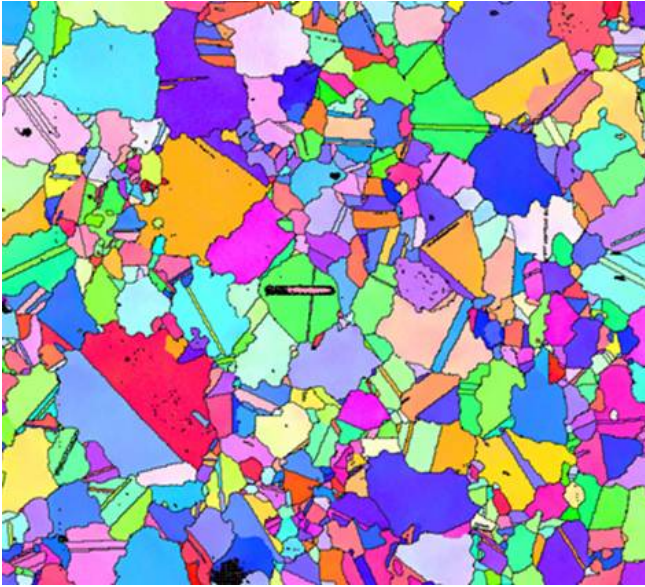


Figure 6: Notch 3 inverse pole figure of local microstructure.

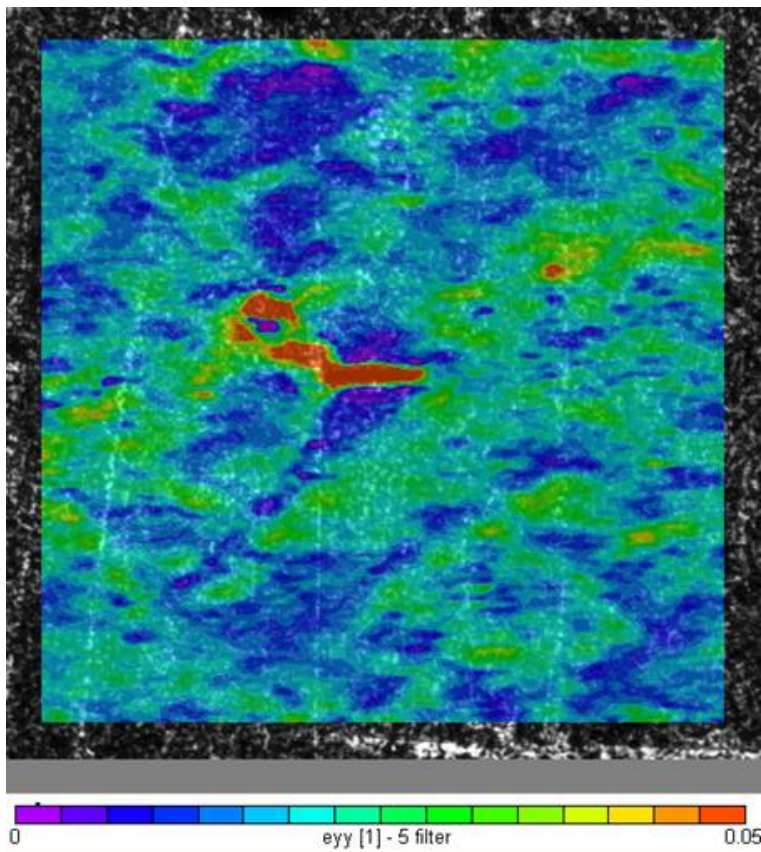


Figure 7: Notch 4 strain distribution at 900MPa



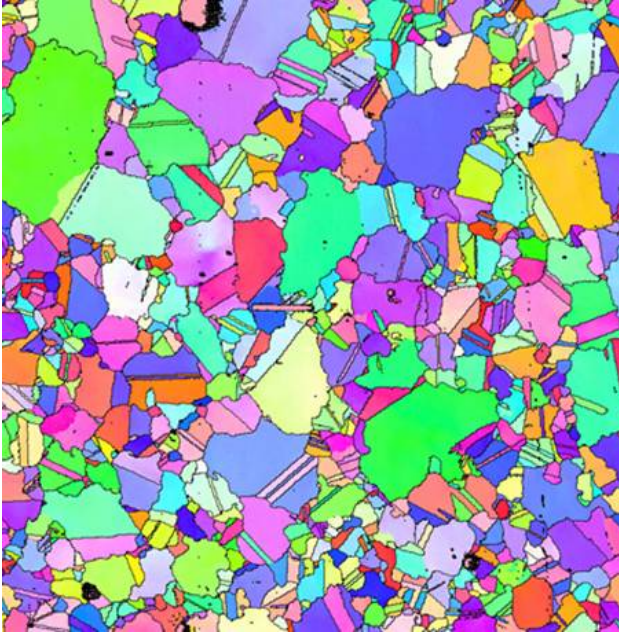


Figure 8: Notch 4 inverse pole figure of local microstructure.

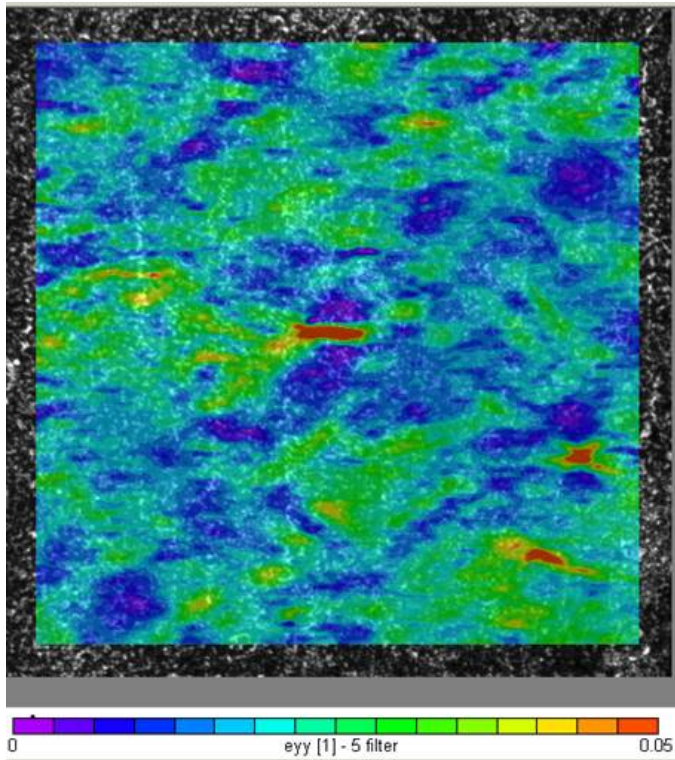


Figure 9: Notch 5 strain distribution at 900MPa

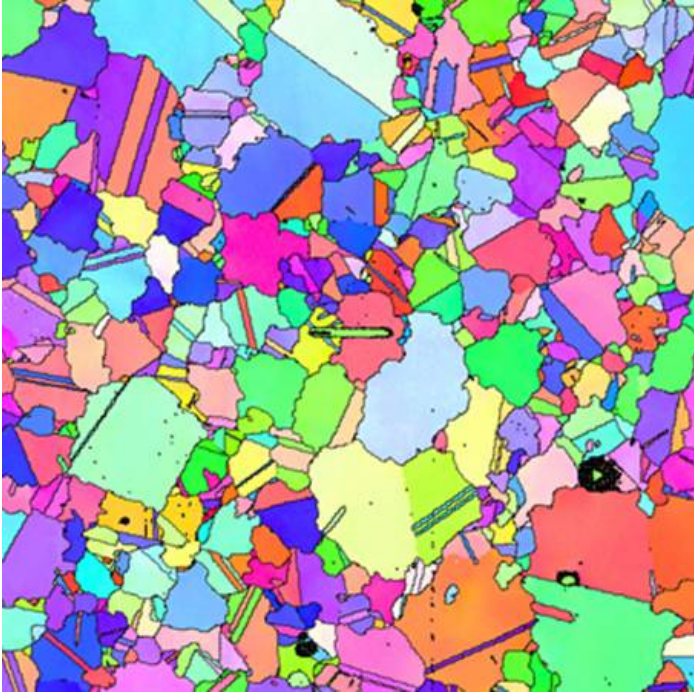


Figure 10: Notch 5 inverse pole figure of local microstructure.

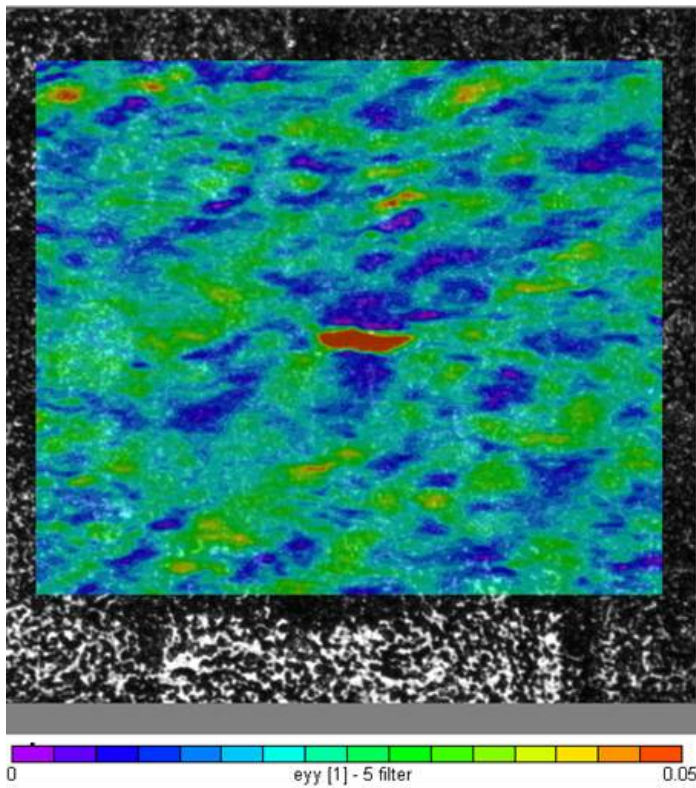


Figure 11: Notch 6 strain distribution at 900MPa



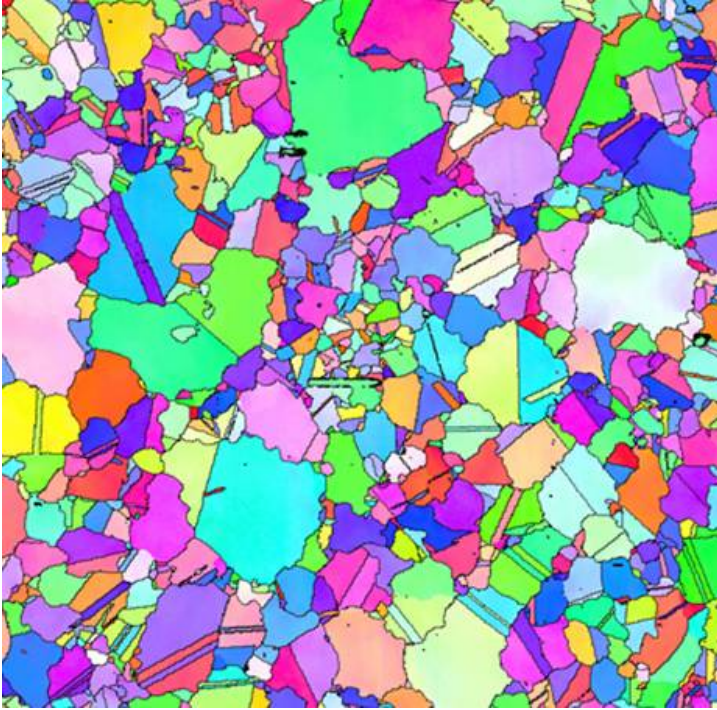


Figure 12: Notch 6 inverse pole figure of local microstructure.

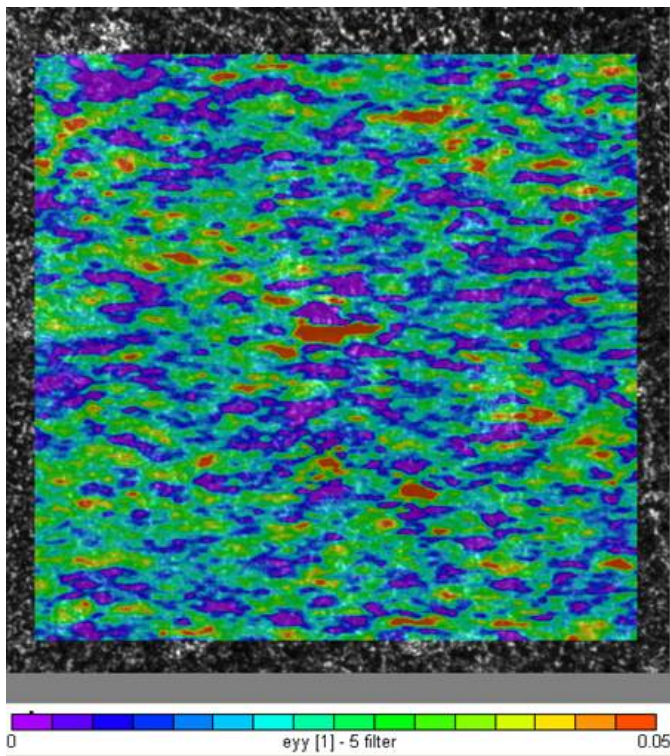


Figure 13: Notch 7 strain distribution at 900MPa

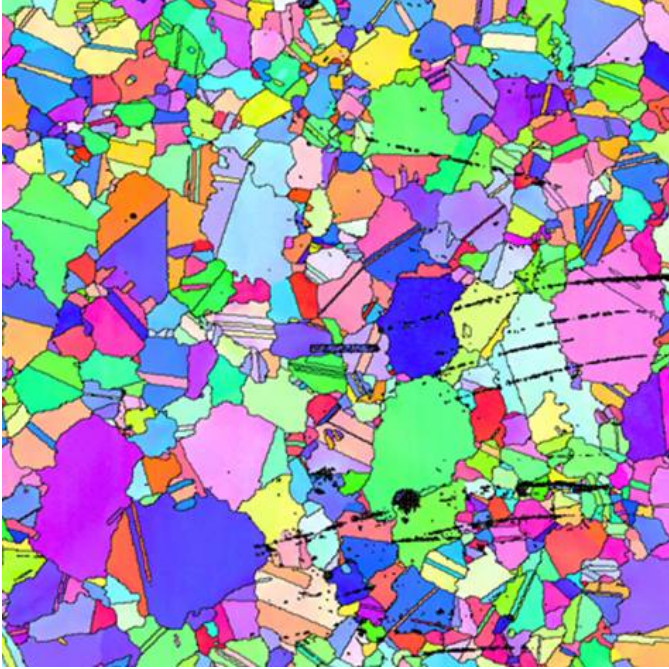


Figure 14: Notch 8 inverse pole figure of local microstructure.

## **In-Situ Tensile testing of Rene 88DT at room and elevated temperatures**

B. B. Bartha<sup>a</sup>, S. Fairchild<sup>b</sup>, T. Murray<sup>c</sup>, M. Tschopp, W. J. Porter<sup>c</sup>

Universal Technology Corporation, Dayton, OH 45433

US Air Force Research Laboratory, Wright-Patterson AFB, OH 45431

University of Dayton Research Institute, Dayton, OH 45431

### **Abstract**

A tensile test of Rene 88 DT was conducted at 70C and 593C inside a Scanning Electron Microscope (SEM). Deformation mapping was conducted on the surface of the specimen during each tensile test. Digital Image Correlation (DIC) was performed on the obtained images to obtain the plasticity near each notch area.

### **Introduction**

Fatigue variability plays a critical role in the determination of the total life in fracture critical components [ref1]. Engine Rotor Life Extension (ERLE) and Materials Damage Prognosis programs under the Air Force have examined various life limiting factors and the potential to extend the lives of in service components. Various material specific mechanisms have been found to contribute to fatigue variability. In titanium, fatigue variability was shown to be due to competing failure mechanisms [ref2]. A divergent failure mechanism has also been reported for Rene' 88DT superalloy [ref 3]. The initiation site size, location of the initiation site and the crystallographic orientation near initiation sites were shown to significantly influence the total fatigue life of Rene' 88DT. (Discuss Supersolvus IN100 fatigue data results to be published).

While previous studies have investigated the fatigue variability of nickel-base superalloys focusing on the location of crack location, the fracture mechanics of a subsequent fatigue crack also plays an important role in determining fatigue variability. The current study focuses on the crystal plasticity behavior in Rene 88DT due to the local microstructure in at room and elevated temperatures.

### Experimental Procedure

A novel in-situ testing technique was developed to obtain the local deformation behavior of Rene 88DT at room and elevated temperatures. The Experimental setup consisted of a Quanta 600 FEG SEM coupled with a Fullam 1000lbs high temperature in-situ loading stage (Figure 1). A specimen was prepared with a gage length was measured to be 0.11in wide and 0.032in thick with a 0.7in gage length (Figure 2). Through thin film ablation TTFA was used to coat the specimen surface with platinum nano-particles, in order to obtain images with enough contrast to conduct image correlation on the obtained secondary electron images (Figure 3-4).

The specimen surfaces were cleaned to a finish 1 $\mu$ m mechanical polish or electro-polished before the platinum deposition. It was vital in these experiments to keep the surface clean of everything for optimum imaging and deposition. The surface microstructure can be seen in the electron backscatter micrograph in Figure 5. TTFA consisted a a 10nm platinum target deposited onto a fused silica plate that was transparent to the laser wavelength of 248nm with an energy density of 0.5 J/cm<sup>2</sup>. The chamber was filled with argon at a pressure of 5 torr.

Each tensile specimen was mounted into the Fullam stage grip fixture and preloaded to 10lbs to allow the specimen to seat and to mitigate specimen rotation. The images were collected at 16 bit depth at a pixel resolution of 4096 by 3773 pixels. The stage controller was turned off during the image acquisition of each load step to minimize distortion effects crated by the motor operating the stage. Each image was focused by raising and lowering the stage fixture in order to keep the working distance the same. If focus is performed with the beam only, rotational artifacts have been detected with DIC.

### Image Analysis

Digital Image Correlation was performed on each image with ViC-2D to calculate the displacement field for each load increment. The image at the 0MPa unloaded condition was used as a reference image for the displacement calculation. A subset size of 99 pixels was used for each calculation with a 5 pixels step size and cubic B-spline interpolation.

### Results

The displacements and strains were calculated with each load step and can be seen in Figure 6. The strain concentrations correlate well to the observed slip bands that can be seen in Figure 7. The slip bands in the region of interest were activated at different load levels, where the slip planes need to be obtained from the Electron Backscatter data seen in Figure 8. A Schmid factor analysis is needed to correlate the Schmid factor values to the local strain concentrations seen from DIC.

Current plasticity models compare closely with the obtained results, and can be used to improve their accuracy. These results are vital in improving the current crystal plasticity models in this area.

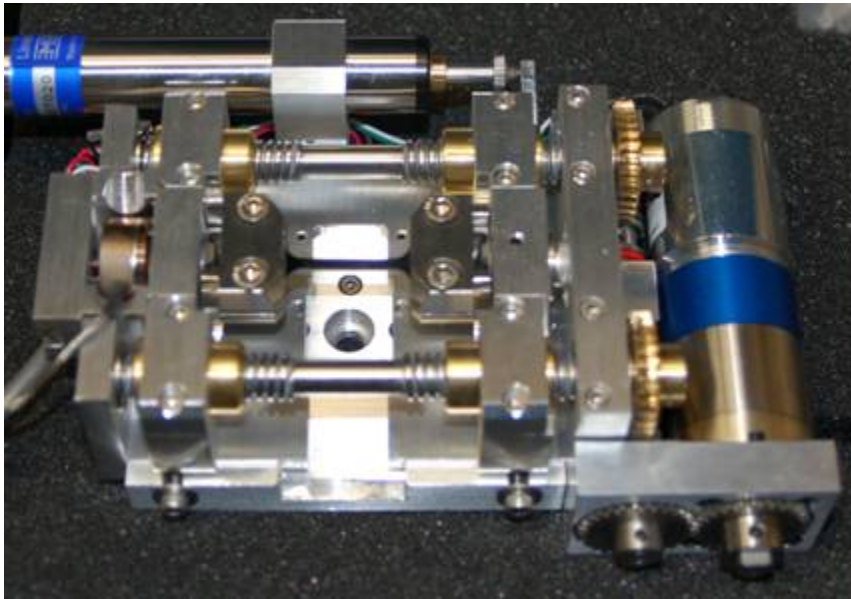


Figure 1: High temperature in-situ tensile stage

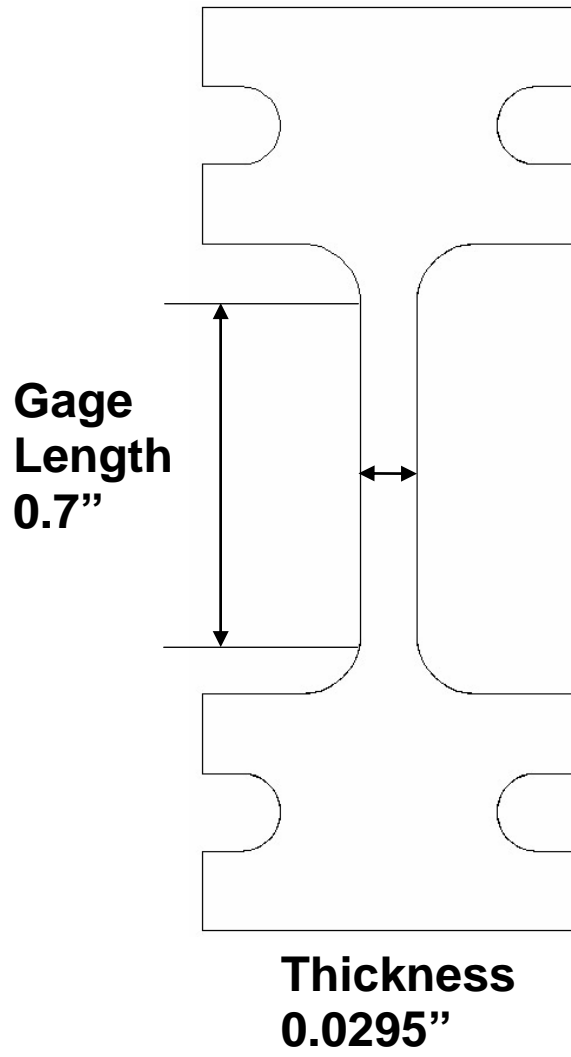


Figure 2: Schematic of tensile specimen



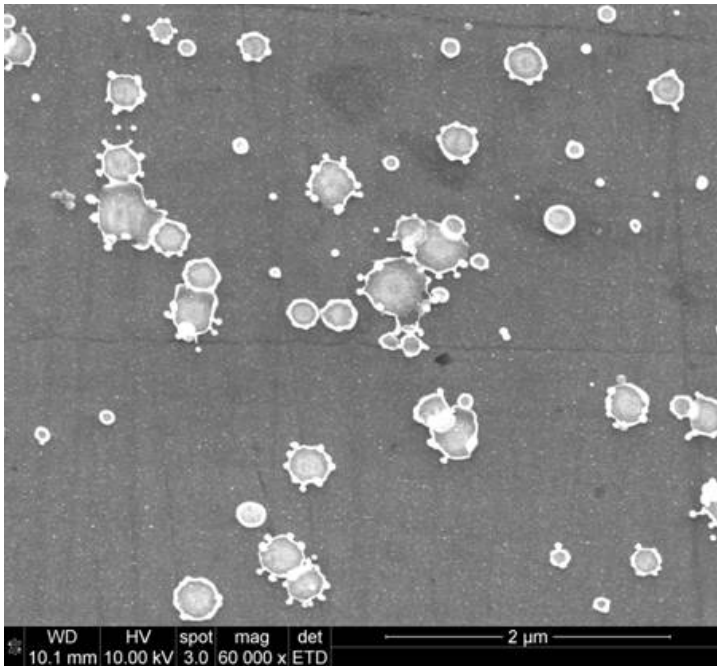


Figure 3: Secondary electron micrograph of platinum deposit on Rene 88 DT surface.

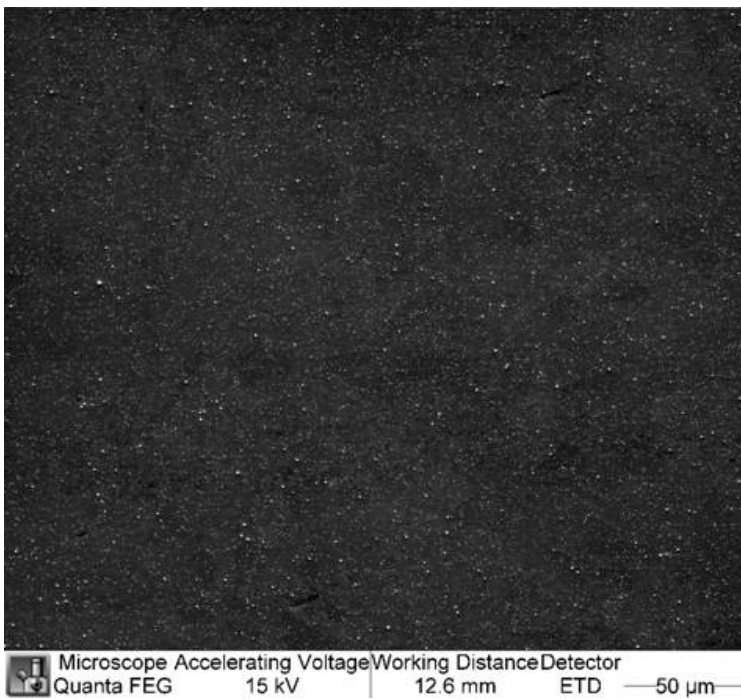


Figure 4: Secondary electron micrograph of the platinum coating used for DIC

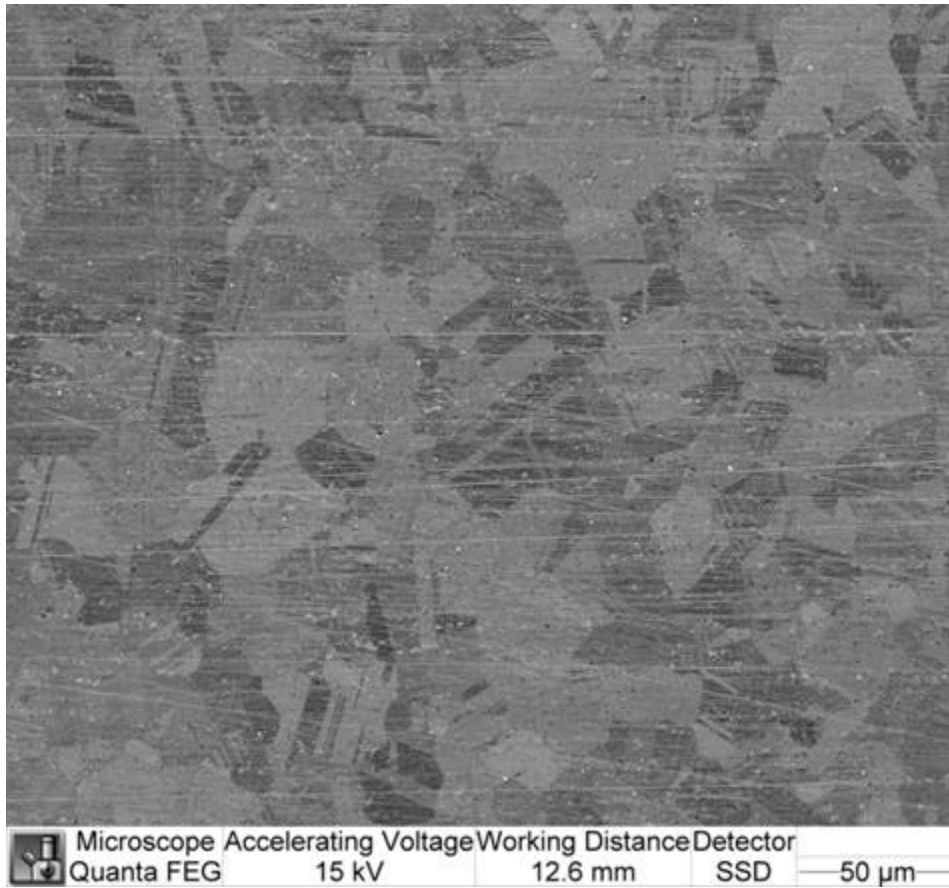


Figure 5: Backscatter electron micrograph showing the local grain structure

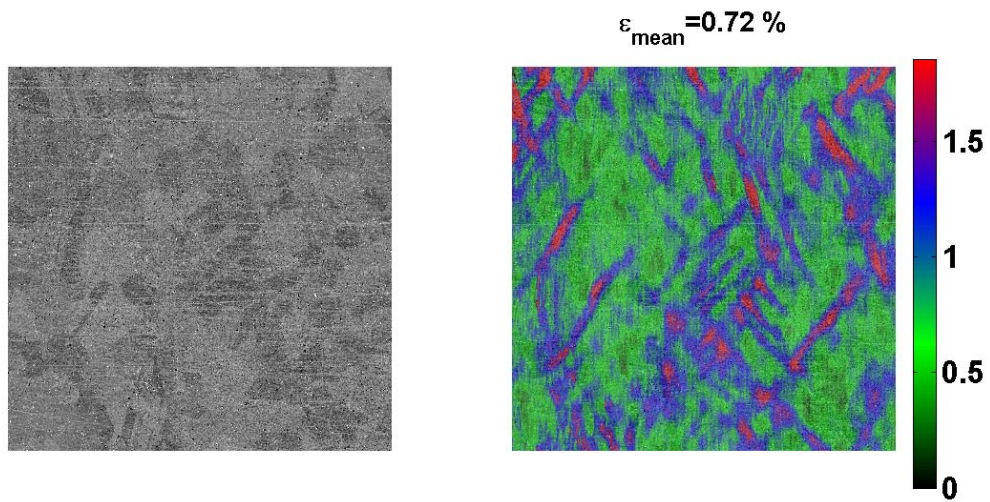


Figure 6: Local strain distribution at 986MPa calculated from



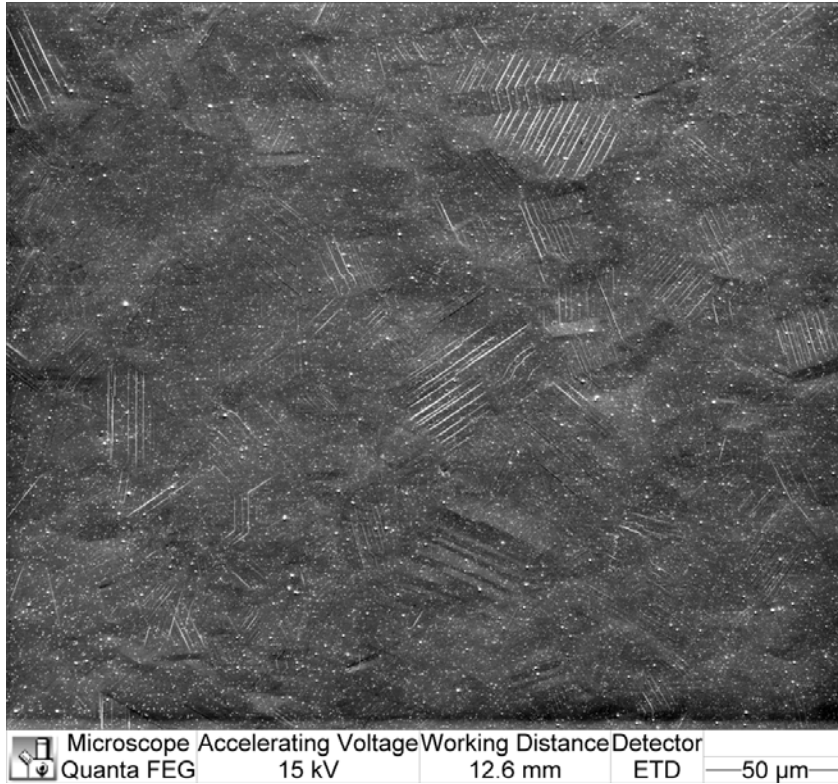


Figure 7: Secondary electron micrograph showing the slip bands formed At 986MPa

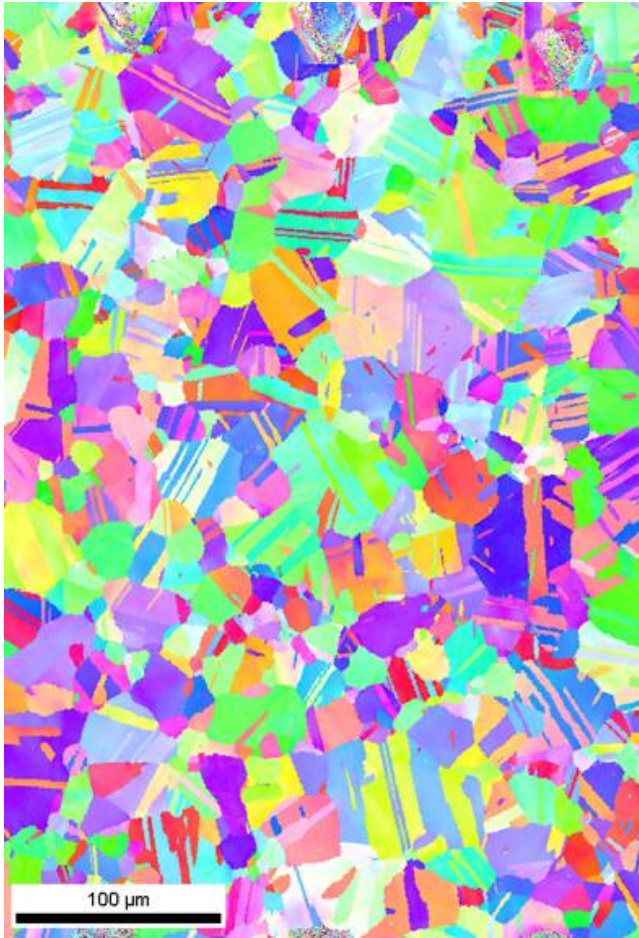


Figure 8: Inverse pole figure showing grain orientation of the deformed area

## Chapter 5

### MICROSTRUCTURAL CONDITIONS CONTRIBUTING TO FATIGUE VARIABILITY IN P/M NICKEL-BASE SUPERALLOYS

W.J. Porter, III<sup>1</sup>, K. Li<sup>1</sup>, M.J. Caton, S. Jha<sup>2</sup>, B. B. Bartha<sup>2</sup>, and J.M. Larsen

AFRL/MLLMN

Materials & Manufacturing Directorate

Air Force Research Laboratory

Wright-Patterson AFB, OH

<sup>1</sup>The University of Dayton Research Institute

<sup>2</sup>Universal Technology Corporation

Keywords: nickel, superalloy, IN100, René88DT, fatigue, variability, image correlation

#### Abstract

Variability in the fatigue behavior of two common nickel-base superalloys is discussed, with emphasis given to understanding the behavior of short fatigue cracks. René88DT and IN100 are the materials of interest and serve important roles in many turbine engine systems. Multiple specimens of each material were tested under low cycle fatigue (LCF) conditions at elevated temperature. Two IN100 specimens that exhibited significant difference in cycles to failure and three René88DT specimens having dissimilar short fatigue crack growth rates were interrogated to determine the reasons for these variations. This paper will discuss the microstructure adjacent to the initiation sites in these specimens and its role in affecting the observed disparate crack growth behavior. Additionally, an image correlation technique, used to evaluate the development of strain concentrations in a René88DT tensile specimen at room temperature, is described. The utility of image correlation for identifying microstructural ‘hot spots’ (i.e. initiation sites) in concert with LCF testing is considered.

#### Introduction

Life prediction models that integrate the inherent fatigue variability of materials used in gas turbine engines are of interest to the USAF. Past research indicates that much of the variability seen in fatigue behavior is related to material response in the presence of small (<100 $\mu$ m) fatigue cracks [1,2]. While extensive databases of long crack growth data exist for nickel-base superalloys, similar databases for small crack growth data are lacking, as is our general understanding of their behavior particularly under LCF conditions. Factors associated with differences in small crack behavior include local microstructural features including neighboring grain (mis)orientation, grain substructure ( $\gamma'$  precipitates), twins, and anomalies such as the presence of inclusions and pores [3-7].

René88DT and IN100 are important alloys in the field of Ni-base powder metal superalloys in turbine engine applications. They are the focus of this paper due to their important role in US Air Force (USAF) propulsion systems. A current focus of USAF materials research pertains to the development of life prediction

methodologies based on determining remnant component capability via prognostic approaches. The ultimate goal of this work is to arrive at a better understanding of those factors central to influencing fatigue variability to aid future USAF life-management efforts.

#### Experimental

##### Material

The alloys investigated in this study were René88DT and IN100. Both are powder metal processed materials that were solution treated above the gamma prime ( $\gamma'$ ) solvus temperature (super-solvus). The sources of material for each alloy were large pancake forgings produced using standard industrial practices. The nominal composition and microstructure of each alloy are shown in Table I and Figure 1, respectively. The average grain size of the René88DT is approximately 30  $\mu$ m (Fig. 1a); the microstructure is highlighted by a large number of annealing twins and very fine  $\gamma'$  phase material that forms upon cooling with diameters on the order of 200 nm (Fig. 1b). Aging or tertiary  $\gamma'$  phase, although not apparent in Fig. 1b, is also present and reported to be approximately 100Å in size [8].

The grain size of the IN100 is approximately 25  $\mu$ m (Fig. 1c). A bi-modal distribution of  $\gamma'$  particles is formed upon cooling from annealing, with the cooling  $\gamma'$  having diameters of 1 $\mu$ m (Fig. 1d) and the aging  $\gamma'$  having diameters of ~ 100nm. Twinning is apparent in the IN100, but not as prevalent as in the René88DT.

The tensile properties corresponding to the temperatures at which the fatigue testing was conducted for each alloy follow. At 593C, the René88DT has a 0.2% offset yield of 985 MPa and an elastic modulus of 176 GPa [3]. At 650C, the IN100 measured a 0.2% yield of 888 MPa, ultimate tensile stress of 1225 MPa, an elastic modulus of 175 GPa, and a strain at failure of 41%.

##### Testing Procedure

Cylindrical dog-bone specimens having a nominal gage diameter

Table 1. Nominal composition of René88DT and IN100 (Weight Percent)

	Co	Cr	Mo	W	Al	Ti	V	N	B	C	Zr	Ni
R88DT	13	16	4	4	2.1	3.7		0.7	0.01	0.03	0.03	bal
IN100	18.5	12.4	3.2		5.5	4.7	0.8			0.07		bal

## Chapter 5

of 6.35 mm were used in this study. The specimens were extracted such that the tensile axes were parallel to the circumference of each forging. All of the specimens were machined to a low stress grind (LSG) finish. The IN100 specimens were tested in the LSG surface condition. To further minimize the effects of surface residual stresses due to machining, the gage sections of the René88DT specimens were electropolished using a procedure described in [3].

The René88DT specimens were tested under load control at 1250MPa, 593°C, a frequency of 0.33 Hz, and a stress ratio of 0.05. All IN100 testing was also done under load control at 1100MPa, 650°C, a frequency of 0.33 Hz and a stress ratio of 0.05. The stress levels chosen for each group of specimens are representative of low cycle fatigue (LCF) conditions.

Replicate testing of René88DT specimens at 1250 MPa using the conditions previously described in concert with the electropolished gage sections resulted in a predominance of surface-nucleated cracking. The surface-nucleated cracking

served as a convenient platform for investigating variable short crack growth rates using acetate replication techniques. Surface replicas were taken periodically (at least every thousand cycles, often more frequently) throughout the tests to monitor crack advance. Replication was done at room temperature and, as such, required the furnace to be shut off and the sample cooled to ambient.

An array of analytical tools was used to examine the role of microstructure on the initiation and propagation of small fatigue cracks. These tools included: 1) a scanning electron microscope (SEM) for fractography and orientation imaging microscopy (OIM) of material at and adjacent to the initiation sites, 2) a focused ion beam (FIB)-equipped SEM to reveal the microstructure in the areas of interest, 3) a software package that enabled quantitative fractographic measurements of the initiation sites and surrounding material (MeX by Alicona Imaging GmbH) [9] and 4) a charge-coupled device (CCD) camera attached to an optical microscope for digital image correlation (DIC).

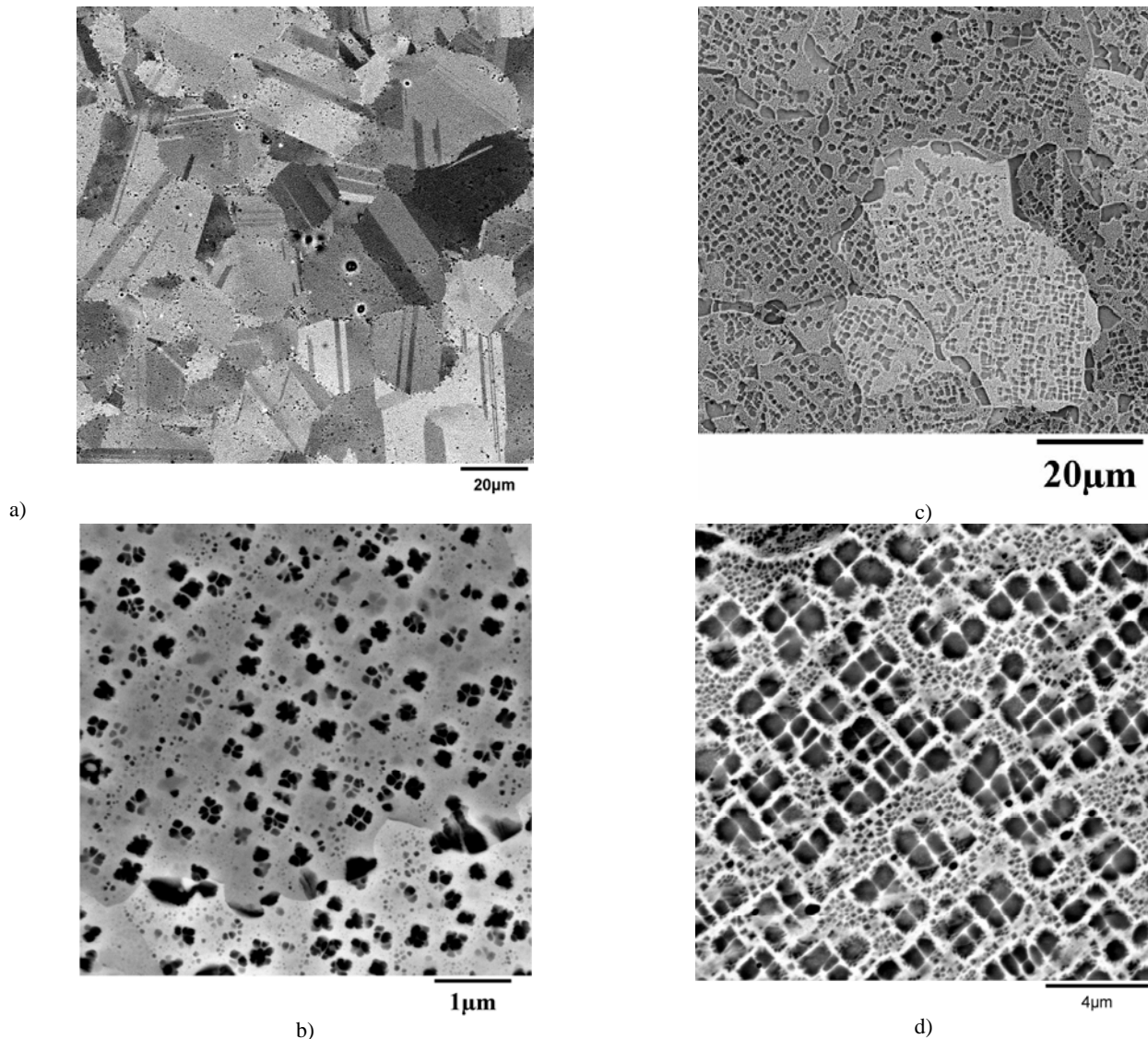


Figure 1. Backscattered SEM images of a, b) René88DT and c,d) IN100 microstructures



## Results and Discussion

### René88DT Fatigue

Surface replicas were used to monitor the advance of short cracks in three René88DT specimens. The initiation site for each of these was found to be non-metallic inclusions (NMI) located at the specimen surface. The lengths of each NMI exposed at the specimen surface are shown in Table 2. The NMIs were similar in size, shape and composition. Fracture surfaces for each specimen are shown in Figure 2. The distinct thumbnail appearance and banding around each initiation site seems to be an artifact of the replication process which required periodic cool down to room temperature. The bands can highlight the amount of crack advance during a given cycle block. However, as shown in Figure 3, for the specimen identified as ‘slow’, there were blocks that showed signs of crack arrest or negligible growth (e.g. from 2000 to 6000 cycles).

Table 2: Information for cracks in René88DT selected for characterization.

Crack ID	Initiation Type	Surface length of initiating feature ( $\mu\text{m}$ )	Cycles to $120\mu\text{m}$
Slow	NMI	35	~7700
Medium	NMI	45	~4500
Fast	NMI	40	~2100

In an effort to correlate fracture surface roughness at crack lengths (2a) less than  $200\mu\text{m}$  to crack growth rate, stereopairs of each fracture surface were collected for input to the MeX software. A three-dimensional representation (digital elevation map) of each surface was created and area-based surface roughness measurements were made. A summary of the surface roughness measurements are shown in Table 3. Using a line-intercept technique, the projected area is the planar measurement of the area of interest (i.e. length x width). An example of a grid placed over the initiation area of the ‘slow’ specimen is shown in Figure 4. The true area is a summation measurement of the changes in topography along the lines of the grid and root mean square (RMS) height is a value calculated by taking the square of the difference in height from a mean height. The qualitative statement, “all else being equal (i.e. material, testing conditions, etc.), the more tortuous a fracture surface, the longer the life” is supported by the quantitative findings reported in Table 3. The trends shown in Table 3, the higher the true/ projected ratio and the higher the RMS value, the slower the crack will advance hold true.

Table 3. Summary of surface roughness measurements near the initiation sites for René88DT specimens.

	projected area ( $\mu\text{m}^2$ )	true area ( $\mu\text{m}^2$ )	Ratio of true/ projected	RMS height ( $\mu\text{m}$ )
Slow	19200	22557	1.175	3.109
Medium	18186	20697	1.138	2.271
Fast	19248	21433	1.114	2.093

As mentioned earlier, variable growth rates exhibited by small fatigue cracks are often attributed to neighboring grain

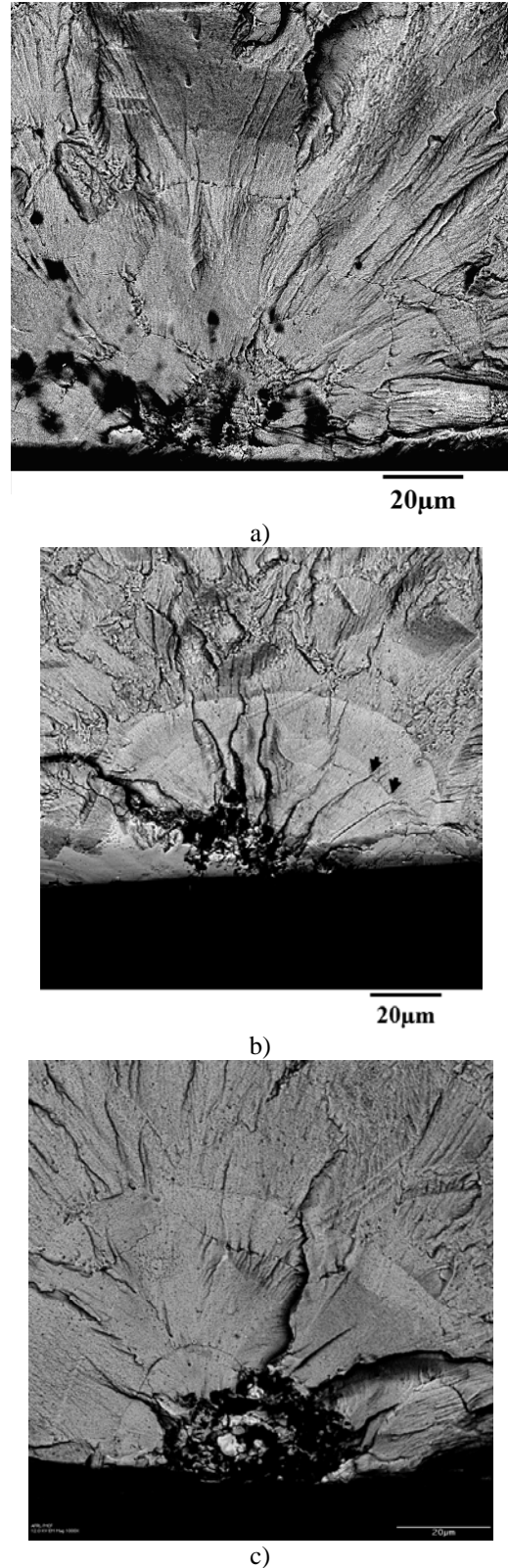


Figure 2. Fracture surfaces and initiation sites from René88DT specimens. a) slow, b) medium, c) fast. Note arrows on b) indicating grain boundary.

## Chapter 5

misorientations. A good example of this is shown in Figure 2b. The arrows on Figure 2b indicate the point at which two river lines terminate, indicating the presence of a grain boundary between two grains with appreciable misorientation. Crack advance is significantly slowed at this point in turn hindering movement of the entire crack front. The crack growth rate slows in this region as shown in Figure 3 for the ‘medium’ specimen from approximately 90 to 100  $\mu\text{m}$  (crack length, 2a, at the surface). This finding is in agreement with location of the arrows in Figure 3b which are found to be approximately 45 $\mu\text{m}$  (crack length, a, for subsurface) from the initiation site.

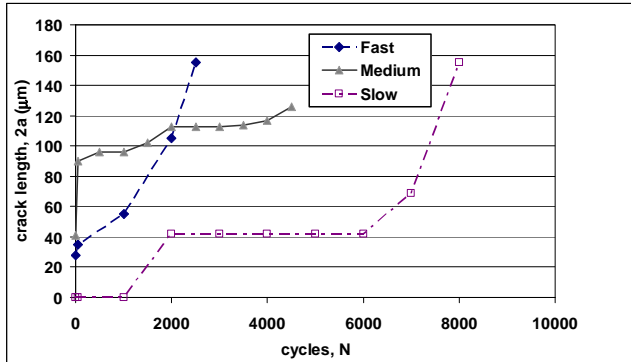


Figure 3. Surface crack size vs N for René88DT.

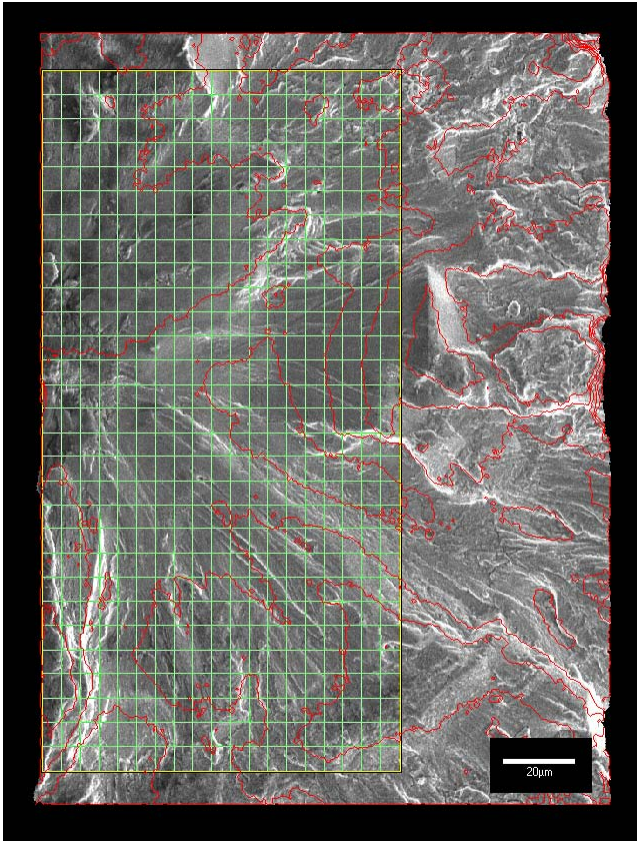


Figure 4. Grid used for line-intercept measurement of fracture surface roughness in René88DT ‘slow’ specimen.

### IN100 Fatigue

Twenty one (21) IN100 specimens were tested in this portion of the study with fatal cracks initiating at either sites of porosity (70%) or non-metallic inclusions (30%). Most of the fatal cracks initiated at the surface of the specimen (60%). due to the large number of pores as compared to NMI, the vast majority of the surface initiated cracks were associated with porosity. From this group, two specimens that initiated at pores on the specimen surface were selected for characterization. While the pore morphology and location within each specimen were very similar, a roughly 4X difference in cycles to failure (5105 vs 23,233) was exhibited. Information about the pores from each specimen is shown in Table 4. One point of interest is that the specimen initiating at the larger pore had longer life.

Table 4: Size and morphology of pores measured in IN100 specimens selected for characterization.

Specimen ID	Cycles to failure	Pore Diameter ( $\mu\text{m}$ )	Pore Area ( $\mu\text{m}^2$ )	Aspect ratio
long life	23,233	32.5	831	1.1
short life	5,105	20.3	326	1.0

The next step was to use the FIB to prepare the material beneath and surrounding the initiation sites for OIM imaging. Figure 5b and e show post-FIB, backscattered electron images of each of the IN100 specimens revealing the supersolvus microstructure. Figure 5c and f show the electron backscattered diffraction (EBSD) images for each specimen.

As expected, given the P/M processing route used for the IN100, the OIM information from each specimen reveals a microstructure with no strong overall texture. The most noteworthy difference in the OIM data between the two specimens is the presence of more twin boundaries in the long life specimen. Efforts are continuing to determine whether this difference in the amount of twinning in the short crack region is a factor contributing to variable fatigue behavior. Other factors under investigation include quantitative analysis using the OIM data of the types of grain boundaries present in the areas of interest. A preponderance of high angle (large misorientation) versus low angle (small misorientation) grain boundaries has been shown to substantially hinder crack growth rates and may play a significant role in fatigue variability.

### René88DT Tensile/ Image Correlation

In addition to the fatigue variability study with microstructure, tensile testing was performed while imaging the deformation behavior of the local microstructure. Electron Backscatter Diffraction (EBSD) was first performed in an area of interest on the surface of a René88DT specimen in order to obtain the local



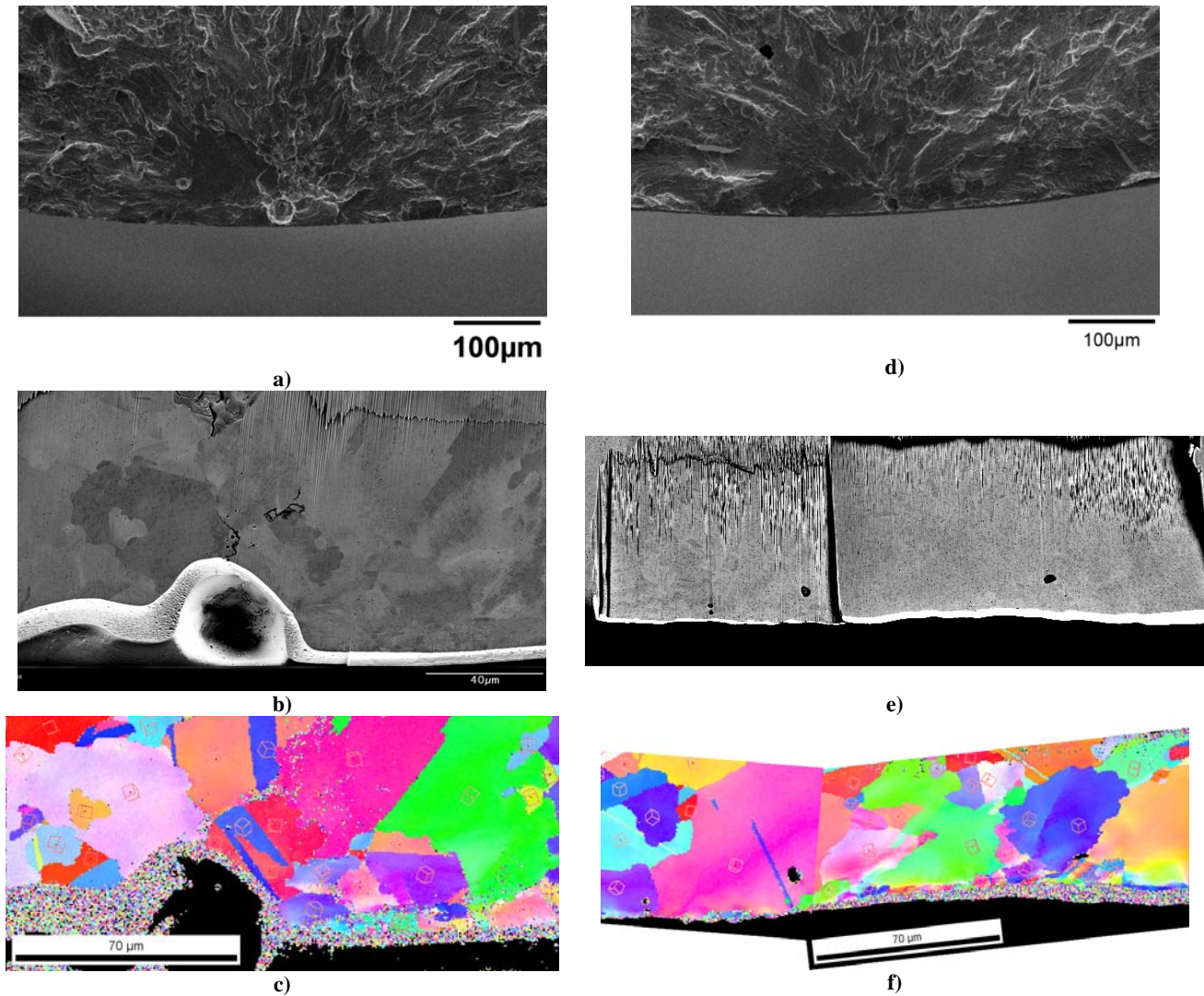


Figure 5. SEM images of the IN100 fracture surfaces before FIB milling, (a, d), after FIB milling, (b, e), and OIM images from the FIB-milled surfaces, (c, f). Figs. a,b,&c) correspond to the long-life specimen; Figs. d,e,& f to the short-life specimen.

orientation (Figure 6). The orientation values were used to obtain the grain boundary misorientation (Figure 7). During the tensile test, images were taken of the area of interest with a CCD camera and an optical microscope. The strain distribution calculated using Vic-2D digital image correlation software (Figure 8) [10, 11]

. The EBSD data was combined with the optical data to compare the effect of orientation on the plastic strains. The highest strain concentrations are located near the boundary of the large grain shown in the image. While several twins within the large grain show elevated strain levels, most of the high strain areas occur near high misorientation angle grain boundaries.

The grain boundary misorientation directly affects the micro-mechanical behavior in the above microstructure. Strain concentrations near twice the mean strain or higher are observed near high angle misorientation grain boundaries. Other factors

such as neighboring grain shapes and sizes and orientation with respect to the loading direction also contribute to the observed elevated strain levels.

Due to experimental limitations, the data presented is on the surface only two dimensional, even though the problem is three dimensional. Therefore, the subsurface grain properties and the out of plane displacements are unknown. While the ability to measure these three dimensional properties would increase the accuracy and the confidence in the experimental results, the trends due to grain boundary misorientation and twinning would stay the same. The twinning also produced some strain concentrations of significance when compared to grain boundary misorientations. Further investigation at higher magnifications is necessary to compare and contrast the local strain behavior of grain boundaries and twin boundaries and their importance in crack initiation and propagation behavior relating to fatigue variability.

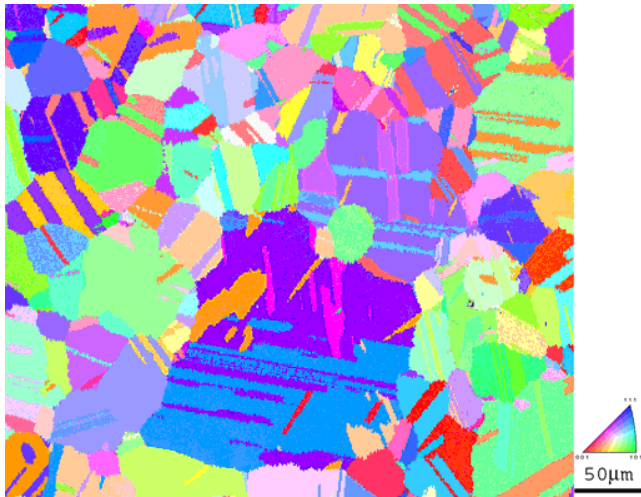


Figure 6: Inverse pole figure of area imaged during deformation mapping.

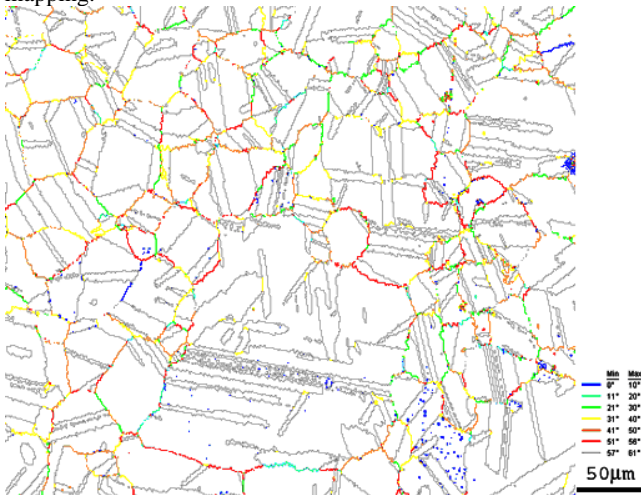


Figure 7: Grain boundary misorientation map near large center grain.

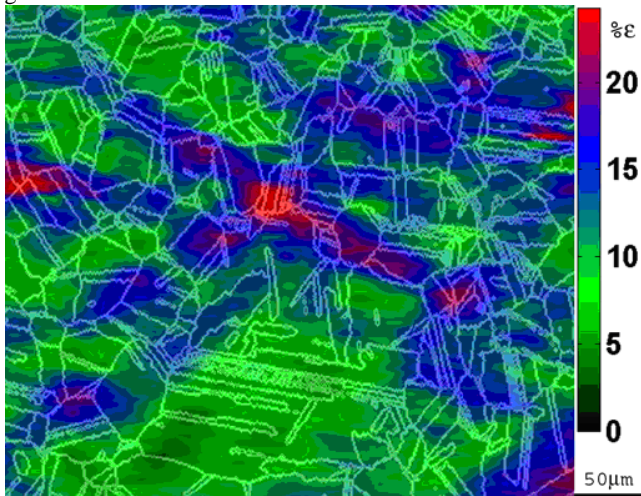


Figure 8: Total strain field of area of interest with a mean total strain at 10% at 1400MPa tensile stress.

## Conclusions

René88DT and IN100 LCF specimens that exhibited dissimilar small fatigue crack growth rates and variable cycles to failure, respectively, were examined to determine the microstructural conditions responsible for each behavior. A digital image correlation technique was employed on a René88DT tensile specimen to determine how and where plastic strains develop during loading.

## References

1. J. Luo and P. Bowen, "Small and Long Fatigue Crack Growth Behaviour of a PM Ni-Based Superalloy, Udimet 720," *Int. J. Fatigue*, Vol. 26, pp. 113-124, 2004.
2. M. Goto and D.M. Knowles, "Initiation and Propagate Behaviour of Microcracks in Ni-Base Superalloy Udimet 720 LI," *Engineering Fracture Mechanics*, Vol. 60, No. 1, pp. 1-18, 1998.
3. M. J. Caton, S. K. Jha, A. H. Rosenberger, and J. M. Larsen, "Divergence of Mechanisms and the Effect on the Fatigue Life Variability of René88DT," *Superalloys 2004*, Edited by K.A. Green, T.M. Pollock, H. Harada, T.E. Howson, R.C. Reed, J.J. Schirra, and S. Walston, TMS (The Minerals, Metals & Materials Society), pp. 305-312, 2004.
4. A. Boyd-Lee and J.E. King, "Short Fatigue Crack Path Determinants in Polycrystalline Ni-Base Superalloys," *Fatigue Fract. Engrg. Mater. Struct.*, Vol. 17, No. 1, pp. 1-14, 1994.
5. M. Marchionni, G.A. Osinkolu, and G. Onofrio, "High Temperature Low Cycle Fatigue Behaviour of Udimet 720 LI Superalloy," *Int. J. Fatigue*, Vol. 24, pp. 1261-1267, 2002.
6. E.S. Huron and P. G. Roth, "The Influence of Inclusions on Low Cycle Fatigue Life in a P/M Nickel-Base Disk Superalloy," *Superalloys 1996*, Edited by R. D. Kissinger, D. J. Deye, D. L. Anton, A. D. Cetel, M. V. Nathal, T. M. Pollock, and D. A. Woodford, The Minerals, Metals & Materials Society, pp 359-368, 1996.
7. A.D. Boyd-Lee, "Fatigue Crack Growth Resistant Microstructures in Polycrystalline Ni-Base Superalloys for Aeroengines," *Int. J. Fatigue*, Vol. 21, pp. 393-405.
8. D.D. Krueger, R.D. Kissinger, and R.G. Menzies, Development and Introduction of a Damage Tolerant High Temperature Nickel-Base Superalloy, René88DT," *Superalloys 1992*, Edited by S.D. Antolovich, R.W. Stusrud, R.A. MacKay, D.L. Anton, T. Khan, R.D. Kissinger, D.L. Klarstrom, The Minerals, Metals & Materials Society, 1992, pp. 277-286.
9. A. Shyam and W.W. Milligan, "Effects of Deformation Behavior on Fatigue Fracture Surface Morphology in a Nickel-base Superalloy," *Acta Materialia*, Vol 52, pp. 1503-1513, 2004.
10. Vogel, D., Gollhardt, A., Michel, B., "Micro and Nanomaterials Characterization by Image Correlation Methods," *Sensors and Actuators A*, Vol. 99, pp. 165-171, 2002.



## Chapter 5

11. Wang, Q., Chiang, F. P., "Experimental Characterization of Interphase Mechanical Properties of Composites," *Composites Part B: Engineering*, Vol. 27, pp. 123-128, 1996.

## **Texture Separation of Alpha and Beta Phases in Duplex Microstructures**

B.B. Bartha\*\*, C.J. Szczepanski, S.K. Jha\*\*, and M.G. Glavicic<sup>1\*</sup>,

Air Force Research Laboratory, Materials and Manufacturing Directorate,

AFRL/MLLM, Wright-Patterson AFB, OH 45433-7817

Rolls-Royce Corporation, Indianapolis, IN

\*UES, Inc., 4401 Dayton-Xenia Road, Dayton, OH 45432

\*\*UTC Corp., 1270 North Fairfield, Dayton, OH 45432

University of Michigan, Materials Science and Engineering, Ann Arbor, MI-48109 USA

### **Abstract**

Electron backscatter diffraction (EBSD) data was obtained for the primary and secondary alpha phases of Ti-6Al-2Sn-4Zr-6Mo (Ti-6246). The results established that the observed microtexture in duplex alloys is a direct result of the prior beta grain orientations, and variant selection. In addition, for a homogeneous duplex microstructure, all of the secondary alpha phase and the majority of the primary alpha grains retain crystallographic coherency, according to the Burgers Relationship, with the surrounding beta-phase matrix which comprise prior beta grains. This investigation develops a unique technique to separate the phases in a duplex  $\alpha/\beta$  titanium microstructure. The image quality map is used to separate the two phases based on the gray level, size and aspect ratio for each phase.

### Introduction

The study of microtexture in duplex titanium alloys with a microstructure that consists of equiaxed (primary) and platelet (secondary) alpha phase that is surrounded by a thin layer of beta phase at ambient temperatures is complicated by several factors. First, in order to examine if there exists a correlation in the crystallographic orientation of the alpha phase constituents (primary and secondary alpha) with that of the beta phase, high resolution EBSD patterns are required to collect a statistically representative number of data from each phase. Second, in some alloys, such as Ti-6Al-4V, where the volume fraction of retained beta phase at ambient temperatures is very low, it is even more difficult to measure the crystallographic orientation of the beta phase.

From a mechanical perspective, microtexture is an artifact of thermomechanical processing that can have a deleterious effect on the fatigue properties of titanium alloys. Recent work examining the role of crystallographic orientation of the primary alpha phase on fatigue behavior has shown that primary alpha oriented suitably for basal  $\langle a \rangle$  slip serves as the fatigue crack initiation sites [1]. Invariably, the microstructural volume surrounding the fatigue crack initiation site was found to be strongly textured for basal and prism slip. Hence from a fatigue life prediction perspective, tools that aid in the understanding of how microtextures develop and the ability to predict crystallographic orientation are essential for the development of life prediction models that incorporate crystallographic orientation into a modeling framework.

The objective of the present work is to use image quality maps to separate the primary alpha phase and the secondary alpha phase and study the texture of the two phase microstructure.

### Results and Discussion

Figures 1-5 show the equiaxed and lath alpha phase obtained from EBSD data. Each set of a set of 4X4 EBSD data in Figure 6 was processed to produce only a set of grains with only equiaxed or lath alpha, and the prior beta grains were predicted using the previous Monte Carlo Method. Figures 7-9 show the predicted prior beta grains from the original microstructure, as well as the equiaxed and lath microstructures only. The lath microstructure clearly shows a large prior beta grain in red. While the equiaxed microstructure only shows a fraction of the coherency of the previous data set. The results show that The equiaxed alpha does retain some coherency to the prior beta phase of the microstructure.

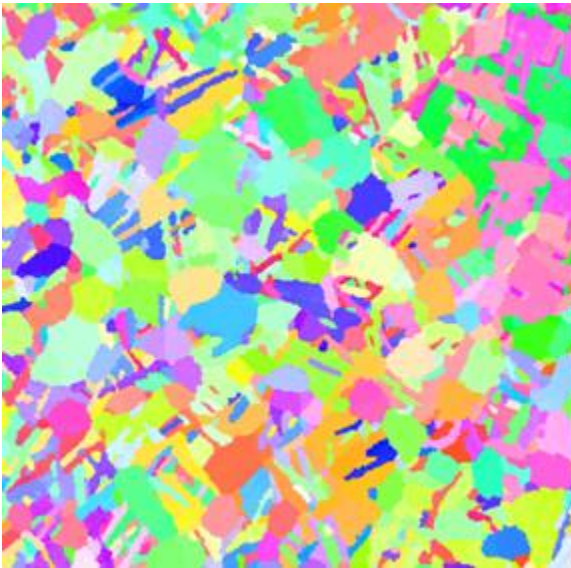


Figure 1: Inverse pole figure showing the grain orientation of a duplex microstructure.

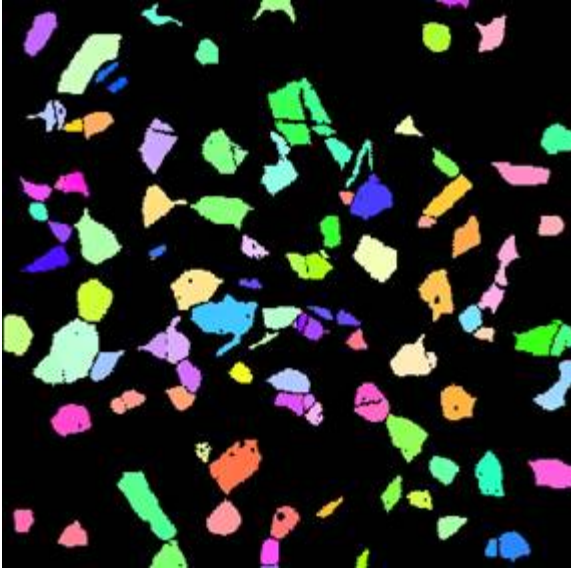


Figure 2: Obtain Euler angle for each primary alpha grain



Figure 3: Equiaxed alpha grains grown from original microstructure

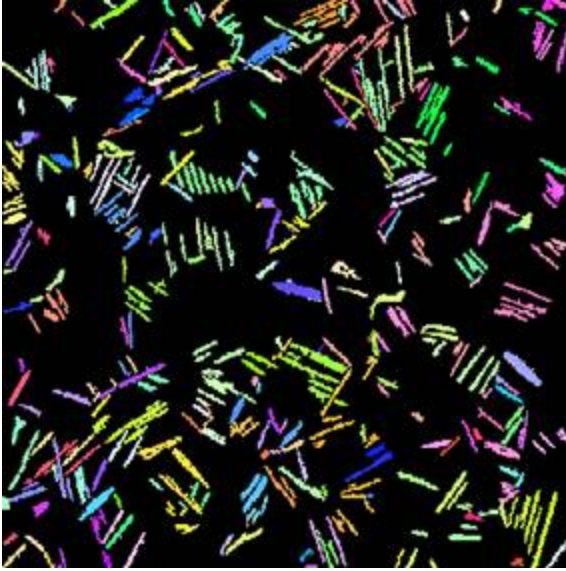


Figure 4: Fill in Euler angles of secondary alpha phase from the original EBSD data.



Figure 5: Lath alpha grains grown from original microstructure.

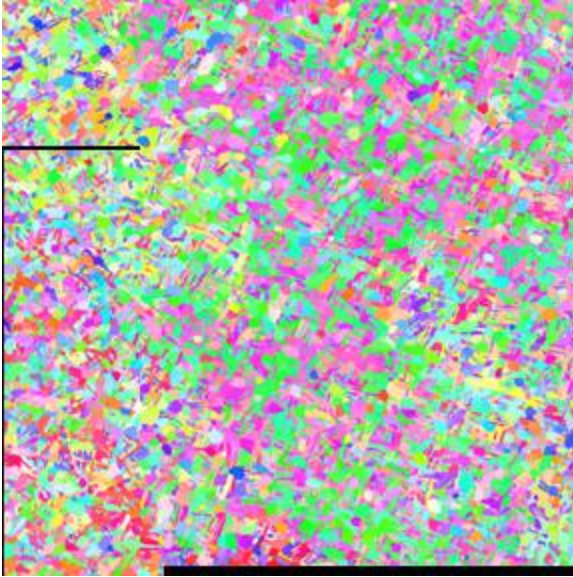


Figure 6: Composite inverse pole figure map of a 4X4 grid of EBSD Data

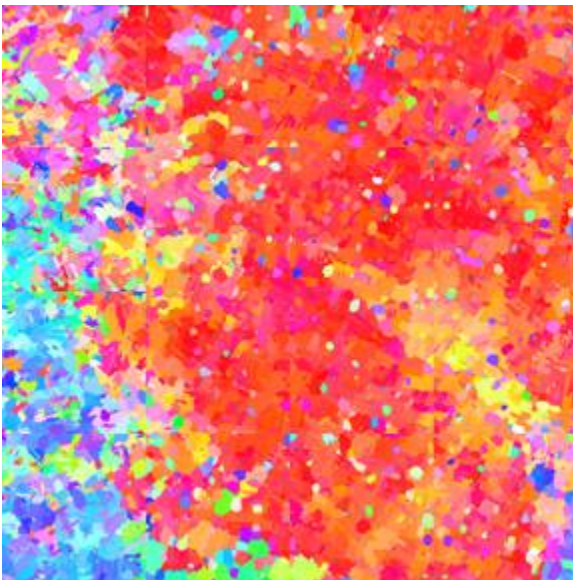


Figure 7: Transformed beta of the entire data set





Figure 8: Transformed beta of the lath alpha grains only

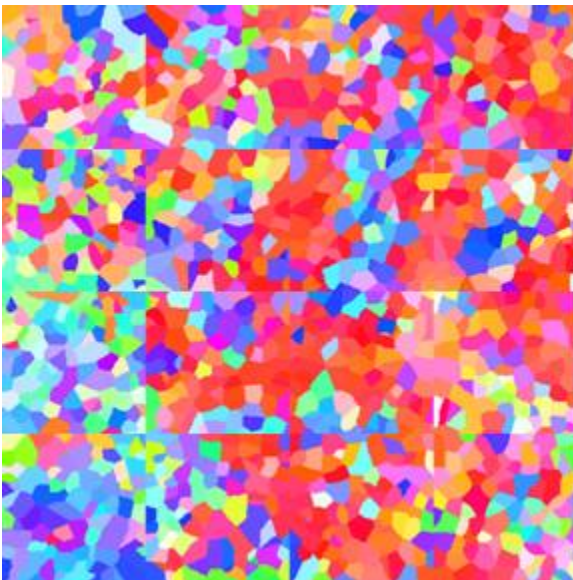


Figure 9: Transformed beta of the equiaxed alpha grains only.

### **References**

- [1] C.J. Szczepanski, S.K. Jha, J.M. Larsen, J.W. Jones. “The role of microstructure on the fatigue lifetime variability in an  $\alpha + \beta$  titanium alloy, Ti-6Al-2Sn-4Zr-



- 6Mo,” in *Fourth International Conference on Very High Cycle Fatigue*, Eds. JE Allison, JW Jones, JM Larsen, RO Ritchie. TMS 2007
- [2] “A Method to Determine the Orientation of the High Temperature Beta Phase From Measured EBSD Data for the Low Temperature-Alpha Phase in Ti-6Al-4V”, M.G. Glavicic, P.A. Kobryn, T.R. Bieler and S. L. Semiatin, *Mat. Sci. Eng. A346*, 50-59 (2003)
- [3] “An Automated Method to Determine the Orientation of the High Temperature Beta Phase From Measured EBSD Data for the Low Temperature-Alpha Phase in Ti-6Al-4V”, M.G. Glavicic, P.A. Kobryn, T.R. Bieler and S. L. Semiatin, *Mat. Sci. Eng. A351*, 258-264 (2003)
- [4] “Validation of an Automated EBSD Method to Deduce the Beta-Phase Texture in Ti-6Al-4V with a Colony-Alpha Microstructure”, M.G. Glavicic, P.A. Kobryn, and S.L. Semiatin, *Mater. Sci. Eng. A385*, 372-376 (2005).
- [5] “A Method to Determine the Texture of the Secondary Alpha Texture in Ti-6Al-4V Duplex Microstructures” M.G. Glavicic, J.D. Miller, and S.L. Semiatin, *Scripta Mater.* 54, 281-286 (2006)

## **Texture Separation of Alpha and Beta Phases in Duplex Microstructures**

B.B. Bartha\*\*, C.J. Szczepanski, S.K. Jha\*\*, and M.G. Glavicic<sup>1\*</sup>,

Air Force Research Laboratory, Materials and Manufacturing Directorate,

AFRL/MLLM, Wright-Patterson AFB, OH 45433-7817

Rolls-Royce Corporation, Indianapolis, IN

\*UES, Inc., 4401 Dayton-Xenia Road, Dayton, OH 45432

\*\*UTC Corp., 1270 North Fairfield, Dayton, OH 45432

University of Michigan, Materials Science and Engineering, Ann Arbor, MI-48109 USA

### **Abstract**

Electron backscatter diffraction (EBSD) data was obtained for the primary and secondary alpha phases of Ti-6Al-2Sn-4Zr-6Mo (Ti-6246). The results established that the observed microtexture in duplex alloys is a direct result of the prior beta grain orientations, and variant selection. In addition, for a homogeneous duplex microstructure, all of the secondary alpha phase and the majority of the primary alpha grains retain crystallographic coherency, according to the Burgers Relationship, with the surrounding beta-phase matrix which comprise prior beta grains. This investigation develops a unique technique to separate the phases in a duplex  $\alpha/\beta$  titanium microstructure. The image quality map is used to separate the two phases based on the gray level, size and aspect ratio for each phase.

### Introduction

The study of microtexture in duplex titanium alloys with a microstructure that consists of equiaxed (primary) and platelet (secondary) alpha phase that is surrounded by a thin layer of beta phase at ambient temperatures is complicated by several factors. First, in order to examine if there exists a correlation in the crystallographic orientation of the alpha phase constituents (primary and secondary alpha) with that of the beta phase, high resolution EBSD patterns are required to collect a statistically representative number of data from each phase. Second, in some alloys, such as Ti-6Al-4V, where the volume fraction of retained beta phase at ambient temperatures is very low, it is even more difficult to measure the crystallographic orientation of the beta phase.

From a mechanical perspective, microtexture is an artifact of thermomechanical processing that can have a deleterious effect on the fatigue properties of titanium alloys. Recent work examining the role of crystallographic orientation of the primary alpha phase on fatigue behavior has shown that primary alpha oriented suitably for basal  $\langle a \rangle$  slip serves as the fatigue crack initiation sites [1]. Invariably, the microstructural volume surrounding the fatigue crack initiation site was found to be strongly textured for basal and prism slip. Hence from a fatigue life prediction perspective, tools that aid in the understanding of how microtextures develop and the ability to predict crystallographic orientation are essential for the development of life prediction models that incorporate crystallographic orientation into a modeling framework.

The objective of the present work is to use image quality maps to separate the primary alpha phase and the secondary alpha phase and study the texture of the two phase microstructure.

### **Results and Discussion**

Figures 1-14 show the step by step numerical procedure that was implemented on each IQ map image in order to separate the primary and secondary alpha phase and the prior beta phase using the gray scale information. The contrast was initially stretched in order to find the gray scale level that separates the primary alpha phase from the beta phase. The subsequent areas were binned and marked with a grain ID, and the size and aspect ratio of each grain was calculated. The results were used to further filter out smaller grains as well as secondary alpha phase grains with a high aspect ratio. The resulting image contained only the primary alpha phase. The Euler angle for each grain was obtained from the original EBSD scan.

The secondary alpha phase was found in a similar manner. Initially the gray level from the primary alpha phase was separated from the original IQ map image. The image contrast was again changed to accurately subtract the beta phase. The smaller grains were again subtracted out, and grains with low aspect ratios were also ignored to find the secondary beta phase. The Euler angles for the resulting grains were obtained from the original EBSD data.

Figures 15-17 show the pole figures of the total image, the primary alpha phase, and the secondary alpha phase that was obtained from the cleaned data set. The difference in the texture in the different phases near crack initiation areas is important to characterize in

order to understand failure mechanisms and to develop accurate life prediction methodologies for duplex microstructures.

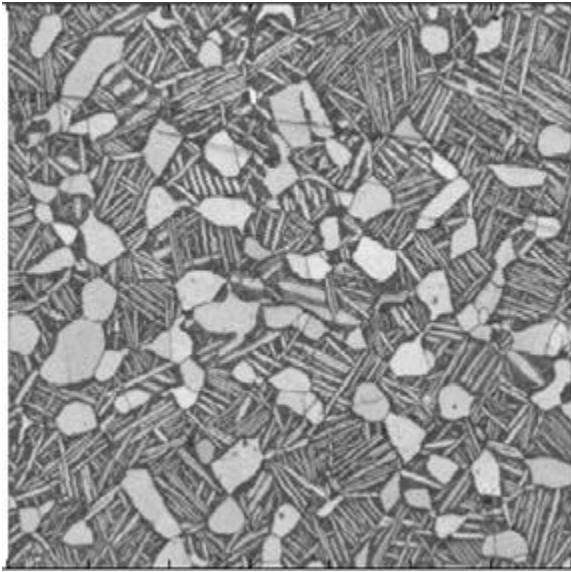


Figure 1: IQ Map of duplex Microstructure.

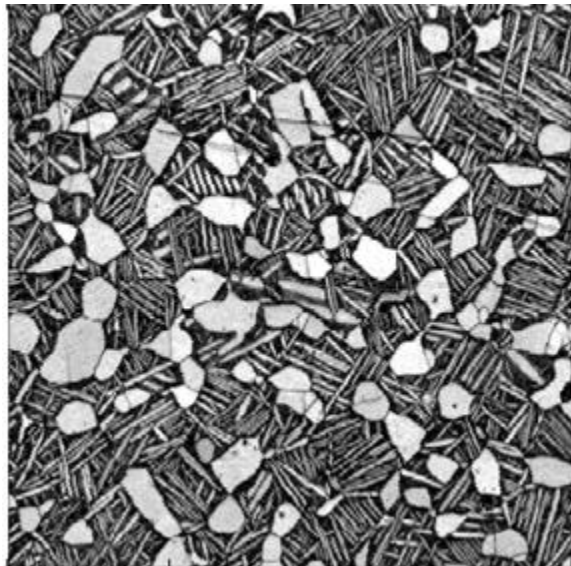


Figure 2: Contrast Stretch o IQ map



Figure 3: Threshold grayscale to obtain alpha phase

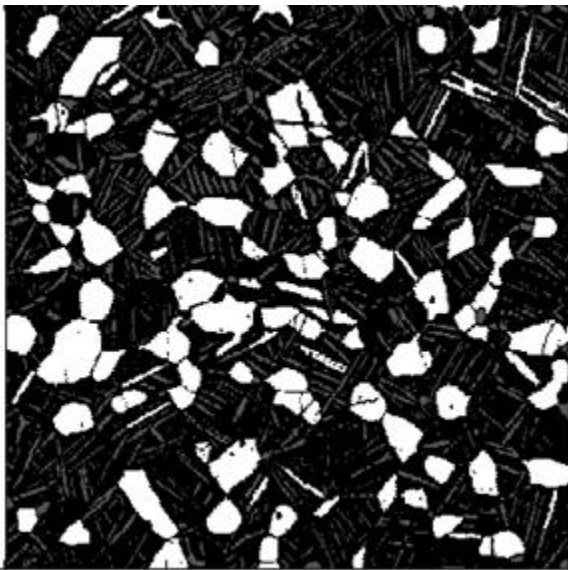


Figure 4: Subtract out small grains

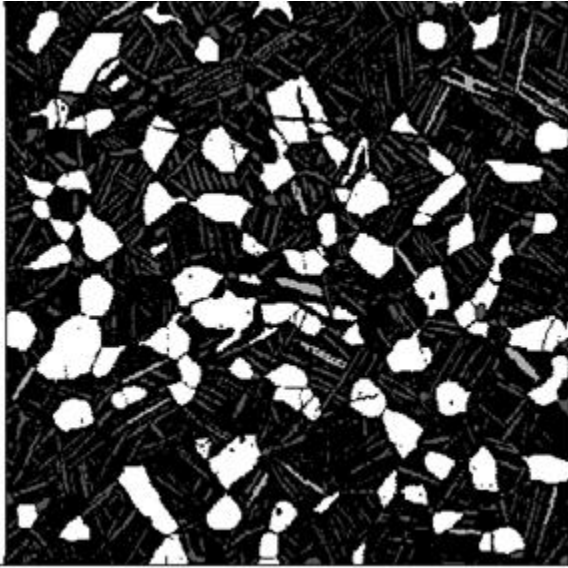


Figure 5: Subtract out grains with high aspect ratios

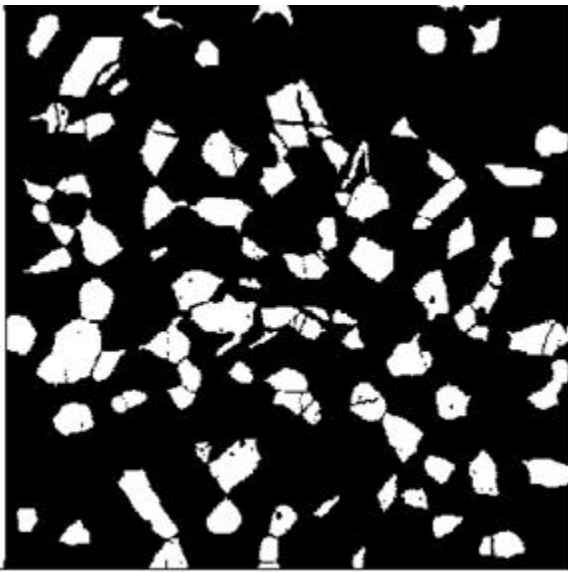


Figure 6: Resulting primary alpha microstructure after image processing



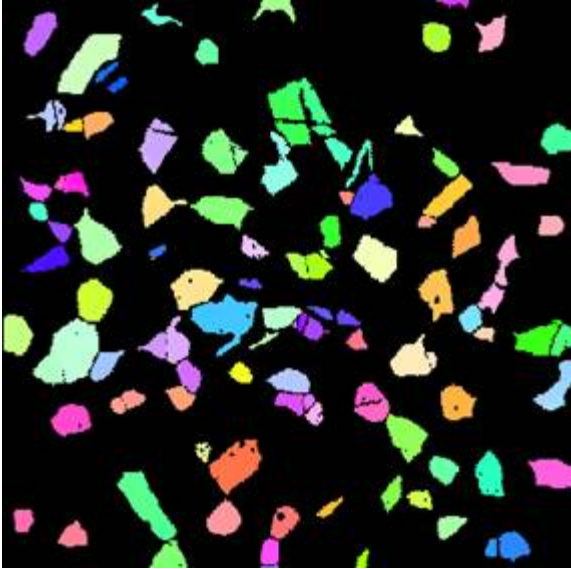


Figure 7: Obtain Euler angle for each primary alpha grain

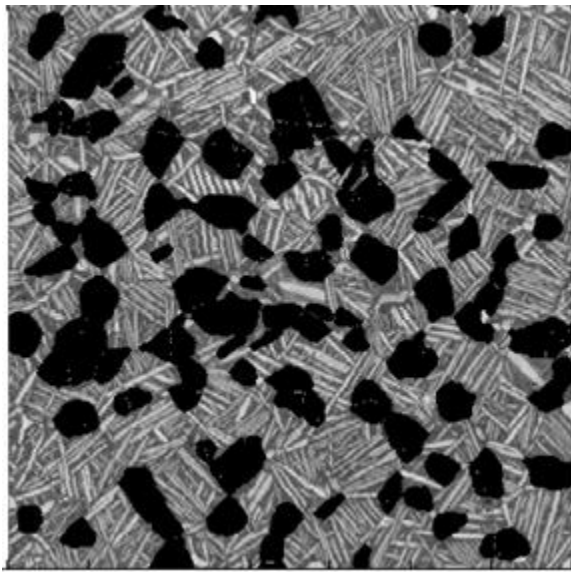


Figure 8: Subtract gray scale values from original IQ map

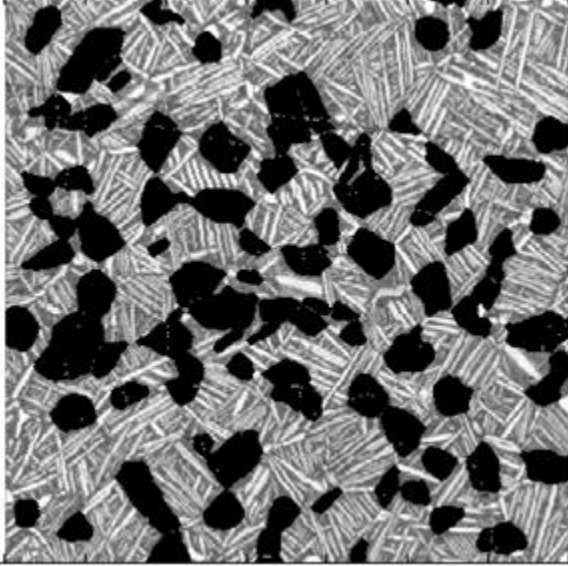


Figure 9: Stretch out the contrast of each image

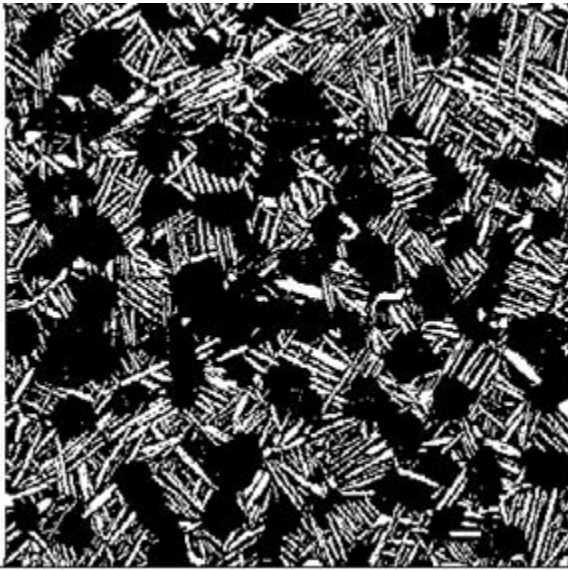


Figure 10: Threshold image to subtract beta phase.

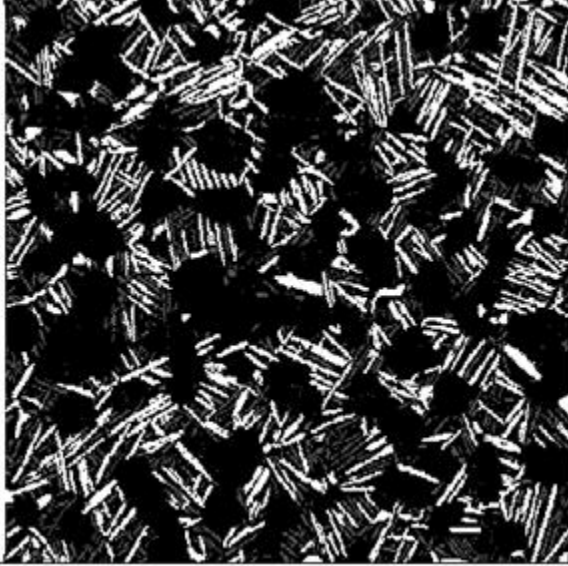


Figure 11: Subtract out small grains

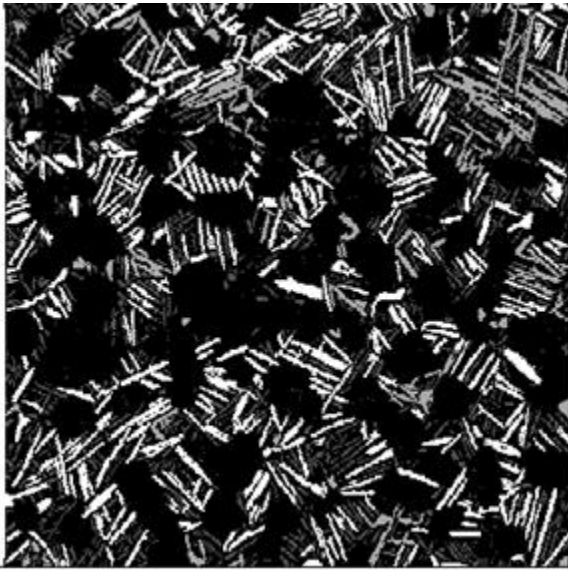


Figure 12: Subtract out grains with low aspect ratios



Figure 13: Resulting secondary alpha phase grains.



Figure 14: Fill in Euler angles of secondary alpha phase from the original EBSD data.

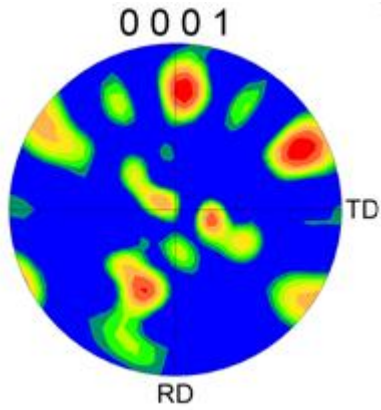


Figure 15: Pole figure of the entire data set.

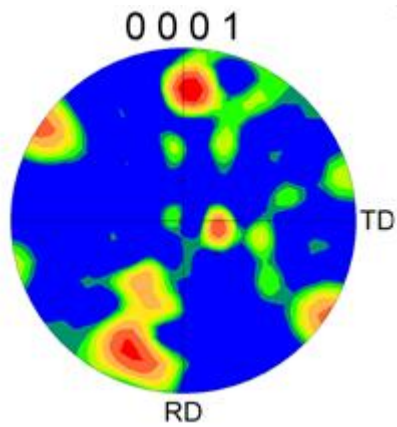


Figure 16: Pole figure of the Primary alpha phase only.

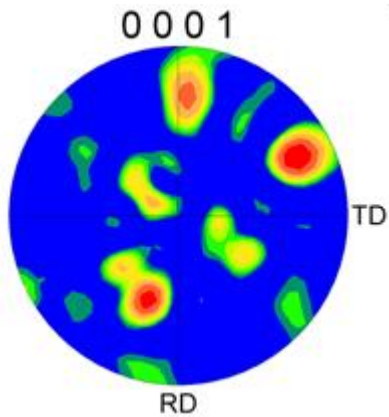


Figure 17: Pole figure of the secondary alpha phase only.

## **References**

- [1] C.J. Szczepanski, S.K. Jha, J.M. Larsen, J.W. Jones. “The role of microstructure on the fatigue lifetime variability in an  $\alpha + \beta$  titanium alloy, Ti-6Al-2Sn-4Zr-6Mo,” in *Fourth International Conference on Very High Cycle Fatigue*, Eds. JE Allison, JW Jones, JM Larsen, RO Ritchie. TMS 2007
- [2] “A Method to Determine the Orientation of the High Temperature Beta Phase From Measured EBSD Data for the Low Temperature-Alpha Phase in Ti-6Al-4V”, M.G. Glavicic, P.A. Kobryn, T.R. Bieler and S. L. Semiatin, *Mat. Sci. Eng. A346*, 50-59 (2003)
- [3] “An Automated Method to Determine the Orientation of the High Temperature Beta Phase From Measured EBSD Data for the Low Temperature-Alpha Phase in Ti-6Al-4V”, M.G. Glavicic, P.A. Kobryn, T.R. Bieler and S. L. Semiatin, *Mat. Sci. Eng. A351*, 258-264 (2003)
- [4] “Validation of an Automated EBSD Method to Deduce the Beta-Phase Texture in Ti-6Al-4V with a Colony-Alpha Microstructure”, M.G. Glavicic, P.A. Kobryn, and S.L. Semiatin, *Mater. Sci. Eng. A385*, 372-376 (2005).
- [5] “A Method to Determine the Texture of the Secondary Alpha Texture in Ti-6Al-4V Duplex Microstructures” M.G. Glavicic, J.D. Miller, and S.L. Semiatin, *Scripta Mater.* 54, 281-286 (2006)

## **Structural Modeling and Weight Optimization of Metallic Honeycomb Sandwich Thermal Protection Systems (TPS)**

B. B. Bartha<sup>a</sup>, P. Martin<sup>b</sup>

Universal Technology Corporation, Dayton, OH 45433

US Air Force Research Laboratory, Wright-Patterson AFB, OH 45431

### **1. Introduction**

Sandwich panels are used extensively in aircraft structures due to the very low weight to stiffness ratios produced using various materials and geometries. Metallic, ceramic and composite materials are each popular in specific loading and thermal conditions where they are the most beneficial structurally, and cost effectively. The application of sandwich panels to Thermal Protection Systems (TPS) for hypersonic flight is currently an area of interest where the use of metallic tiles may be advantageous due to the high damage tolerance of the material over ceramics and composites that are in use for TPS systems. The performance of the metallic tiles must be determined and compared to existing TPS, and the cost effectiveness of metallic panels needs to be investigated to find if metallic TPS is a viable option over current ceramic and composite materials.

Various modeling and characterization techniques on metallic TPS panels are needed to determine their performance and mechanical behavior. The results, in turn, can be used to determine the optimum weight and shape of these panels. Extensive research is available covering structural modeling using methods from the theory of elasticity as well as Finite Element Methods (FEM). The modeling efforts include structural models based on sandwich property and geometry, loading configurations based on mechanical and thermal loads and attachment boundary condition issues. Dynamic issues such as vibrations, fatigue, and impact are also areas of interest for modelers and designers. The results from these models aid designers choose the correct material, panel shape, for a particular attachment and mechanical and thermal load state.

In order to develop structural models for weight optimization of honeycomb panels, it is necessary to understand currently available modeling techniques and conditions that drive models as they relate to metallic TPS panels. The relevant modeling and characterization techniques can be chosen, modified and further developed for weight optimization of metallic TPS panels.

### **2. Background on Modeling Techniques**

Modeling of sandwich panels has been developed using theory of elasticity with beam theory. The equations from beam theory give accurate description of the displacement and stress fields of sandwich and honeycomb structures for various boundary conditions and load cases. The results have been used to analyze bending, buckling and wrinkling failure criteria [1]. In addition, anisotropy, dynamic effects, as well as thermal and



moisture effects have been developed to solve more complex issues for composite materials and added boundary conditions [2]. Layered and non-linear analysis have also been applied to anisotropic layered composites [3]. Most models for specific applications apply specific cases of these theories, incorporating specific conditions that are important for each application that the basic theories may not account for accurately. These advances in the field have been reviewed periodically over the years [4]. The overview of the different sections of the field is presented here to emphasize the issues that arise in honeycomb structures, and the possible role that they play in weight optimization problems.

### **Static Loads**

Honeycomb structures have superior strength under bending and compressive load configurations because they exhibit their largest strength in out of plane loading. Buckling and bending are common modes of failure in these loading configurations. The structural behavior of these modes have been modeled using plates and shells in FEM as well as approximated analytical solutions [5, 6]. Several failure modes such as yield, shear or wrinkling from 3-Point bending of the honeycomb structure can also occur for various effective density and core thickness configurations [7]. In addition, plasticity solutions have also been developed in conjunction with elastic models to predict the macroscopic deformation behavior of sandwich panels incorporating kinematic hardening and softening [8]. Many of the analytical models have been validated experimentally using three and four point bend fixtures to a high degree of accuracy [9]. The relative density of the honeycomb panels also directly correlates to the buckling stiffness [10, 11].

Ultimate stress conditions are also applied to existing elastic models to investigate and address shear, buckling, debonding and fracture failure modes [12]. When 3-D triaxial loads are applied to honeycomb structures, various modes of failure dominate depending on the shape and the orthotropy of the sandwich structure [13]. Asymmetry of the cellular structures has a significant effect on the strength of structures that is tied to apparent density the composite [14]. More complex curved sandwich panels have also been used for structural leading edge applications. Computational models are used for panels that these exhibit unique 3-D properties [15].

### **Dynamic Loads**

Honeycomb panels may undergo cyclic loading that can cause failure in the panels or fastener attachments. In some of these cases, the stress field is found with beam solutions while approximating the fatigue properties using Paris law for crack propagation, Basquin law for high cycle fatigue and Coffin-Manson law for low cycle fatigue [16]. Other properties of sandwich panels relating to fatigue strength of fasteners attachments have also been investigated experimentally [17]. The inherent mechanical behavior of the material used for honeycomb panels in these cases needs to be determined before the use of the above modeling techniques.

Modeling the load history of honeycomb panels subjected to impact loading is needed to determine the damage tolerance of the panels. Considerable work has been conducted on the vibrational behavior of sandwich panels from impact to dynamic response. Both experimental and analytical studies have been conducted investigating the free vibration of honeycomb panels [18]. There have also been studies on the strength of various honeycomb panels subjected to impulse loading and designs of optimum sandwich cores for shock resistance [19]. The vibrational response of these materials can also be modeled using Timoshenko beam theory, as well as relating the response to the material elastic constants [20].

Honeycomb structures are also used in thermal applications such as heat exchangers. In these cases, it is important to understand the thermomechanical characteristics of the material in addition to the strength of the structures because there is usually an inherent tradeoff between the performance of each behavior [21]. Large thermal gradients can also cause large deformations and thermal strains on panels that lead to failure. In these cases the value of the Coefficient of Thermal Expansion (CTE), and structural heat capacity must be chosen carefully for each material in order to mitigate out of tolerance deformations, and to avoid debonding issues that are associated with composite materials.

### **Materials**

Composite materials, as well as layered and smart structures such as piezoelectric honeycombs are heterogeneous and difficult to model, and need modifications to analytical methods to solve for the displacements and stress fields [22]. Homogenization methods have been used in these cases for unit cell composites [23, 24]. These models convert the heterogeneous properties of the composite honeycomb structure to a homogeneous effective elasticity tensor and plate properties. Laminate plate theory assumptions are used in applications where multiple layers and materials are used to build honeycomb panels [25, 26]. Strain energy and weight function methods can also be used to model composite structure behavior along with the homogenization methods for single unit cells [27].

Metallic sandwich structures are advantageous because of their strength to weight ratios are combined with their added damage tolerance over composite and ceramic structures [28]. Improved strength in metallic honeycomb structures for bending and buckling resistance can also be gained with filler foam cores instead of only thickening column walls [29]. The combined strength and thermal characteristics are advantageous for specific applications where the structure must have multi-purpose use [30].

### **TPS Applications**

Metallic TPS have shown to have a promising combination of thermal and structural performance characteristics that are applicable in space vehicle applications [31, 32]. Weight optimization of metallic TPS is an important factor when comparing existing ceramics and composites [33]. In addition, the thermal performance of the metallic TPS must be considered making sure the material does not operate above critical

temperatures, and has proper CTE, heat capacity, and heat flux characteristics. Thermal bending and heat shielding caused by the high surface temperatures and subsequent steep subsurface temperature gradient are issues that must be considered in TPS designs. In addition, attachment issues relating to the performance of the panel attachment region, and the cost effectiveness of replacing TPS panels with particular attachments need to be resolved.

A combination of the above modeling techniques can also be used to develop weight optimization models to obtain the correct material and sandwich configurations for several loading cases [1, 34]. Many parameters can be varied such as honeycomb geometry, while others such as the material properties can be fixed to optimize the problem [35, 36, 37]. Studies have shown that analytical solutions for optimum design can be obtained if the constraints are up to three parameters for certain cases, and numerical analysis is needed when considering additional variables [38].

### **3. Weight Optimization Application**

The development of a comprehensive weight optimization model for honeycomb sandwich TPS must include the main factors that drive the performance of the panels. It is vital to the accuracy of the model to know the panel geometry, the type of attachments, as well as the input structural and thermal loads on each panel. These geometrical and load variables define the boundary conditions for both elasticity and finite element based models. The knowledge of mechanical properties of the chosen materials is needed to predict the stress state of the panels for each boundary condition. The performance characteristics are needed to predict the failure locations for a particular stress state. The combined variables of these configurations and material properties determine the panel material, geometry, and weight for this application.

Initially, elasticity based beam theory for honeycomb panels will be used to optimize the weight of the honeycomb panel similar to previous work performed for TPS [31]. The constraints will include peak stress values for bending and buckling failure modes. The optimization model will also need to account for attachment boundary conditions by using pinned, fixed or free boundary conditions that change the peak stress level for a given load. Structural and thermal loading input boundary conditions can then be included in the model by including point, and distributed loads, as well as thermal strain and thermal gradient effects. Variation in material properties will need to be included using FEA for more complex models. Commercial software package such as ISight will be used to optimize the weight for a particular set of the described input variables using numerical routines such as the downhill simplex method.

Many of the variables used in the described weight optimization scheme must be constrained to obtain a feasible solution. The results of the research efforts from AFRL/ML, AFRL/VA and industry will aid in choosing if variables such as materials and temperatures can be constrained, and determining input bounds such as web and panel thickness. The resulting weight optimization model will, in turn, provide a tool to determine the structural feasibility of using metallic TPS that is competitive with

materials used in current applications. The model will act as a design tool to determine optimum attachment configurations, and material usage for TPS applications.

### Weight Optimization Trade Study With Hypersizer

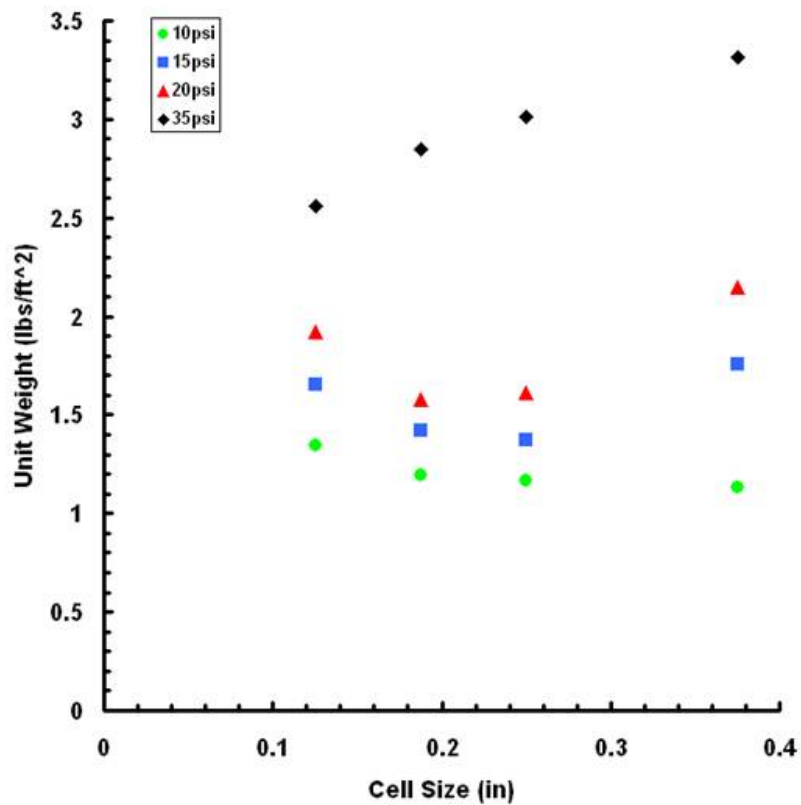


Figure 1: Unit Weight of a 30 in IN617 panel with various cell sizes under increasing normal pressures.

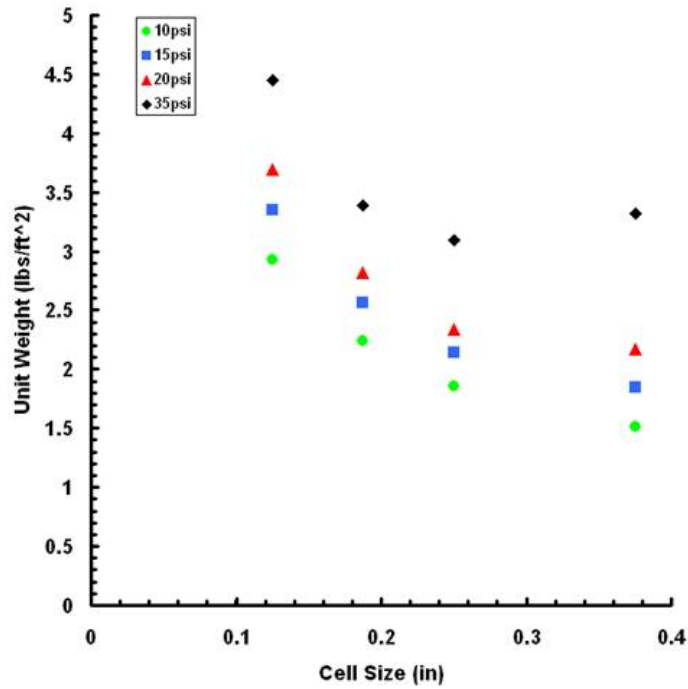


Figure 2: Unit weight of a 30 in IN617 panel with various cell sizes under increasing normal pressures for a 0.1 in normal constraint.

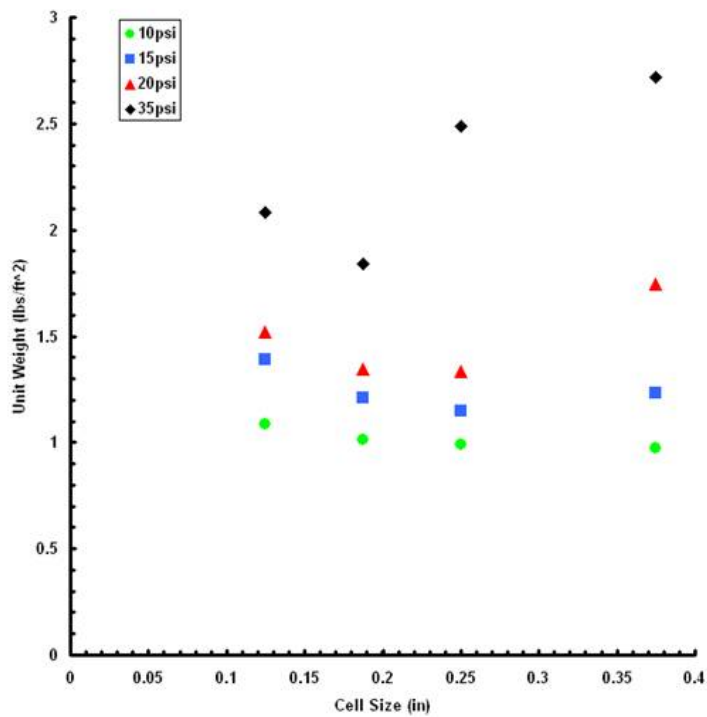


Figure 2: Unit weight of IN617 panel various cell sizes under increasing normal pressures for a 24in square panel.

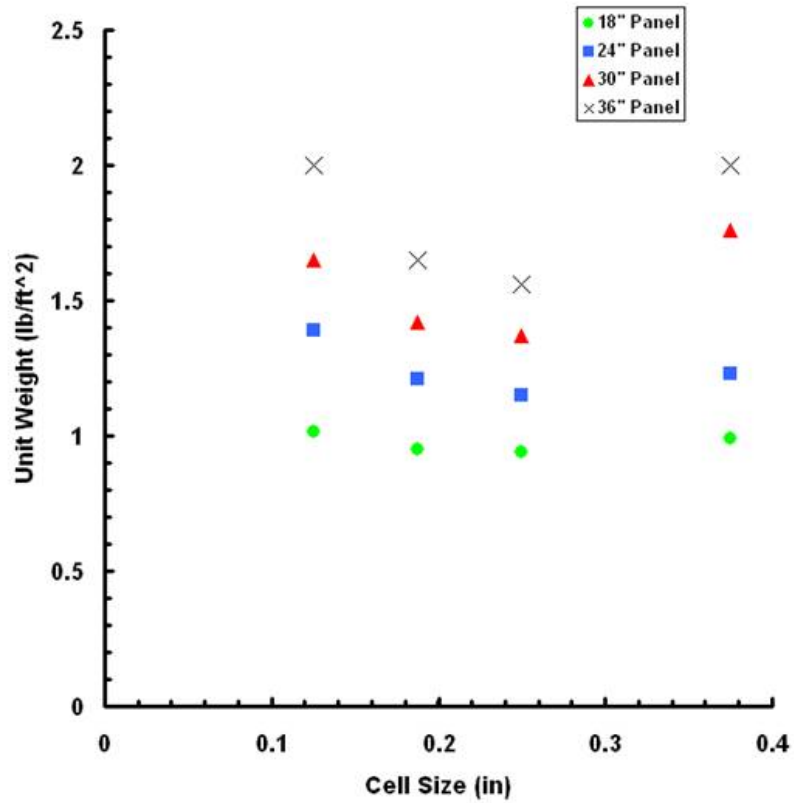


Figure 4: The optimum weight for panel sizes between 18-36in

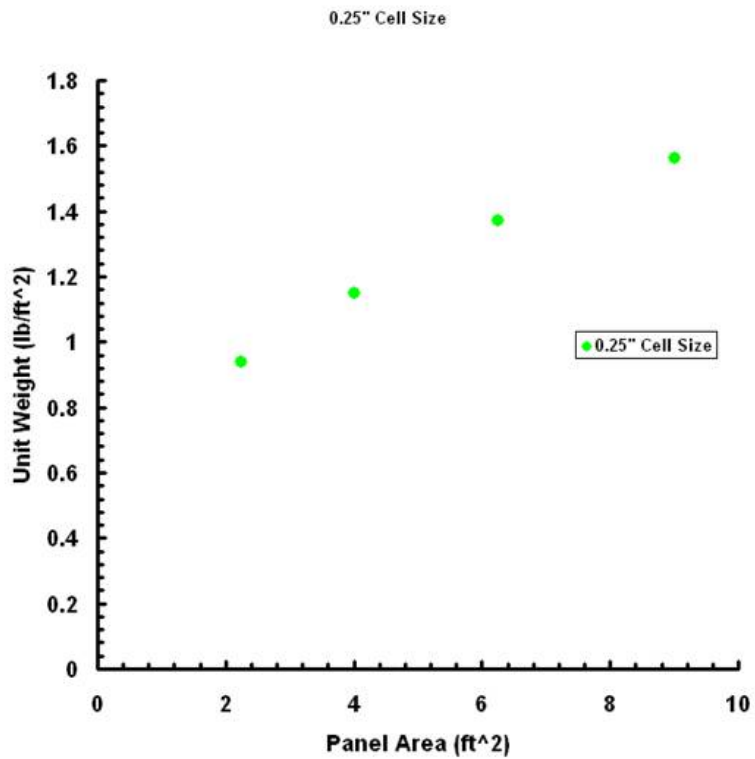


Figure 5: Unit weight is shown to increase with panel area for the panel sizes shown.

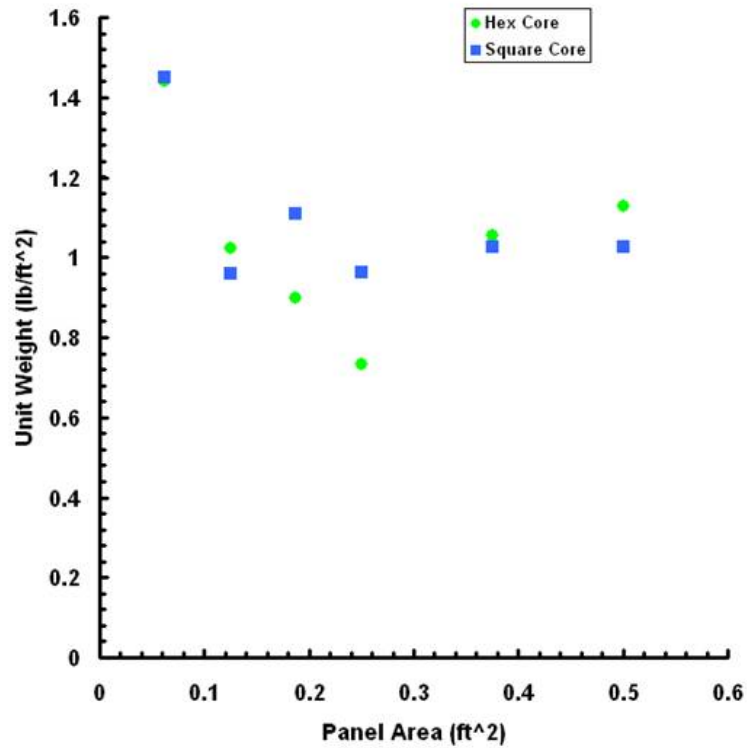


Figure 6: Unit weight is little changed for hexagonal versus square core.

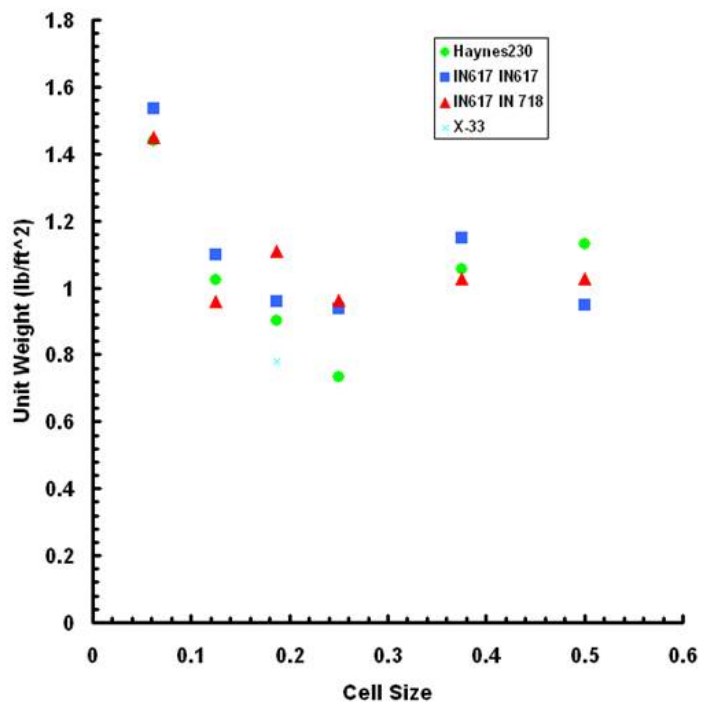


Figure 7: The unit weight for several metallic TPS materials is compared to the tile unit weight used under the X-33 program.

## References

- [1] Allen, H. G., Analysis and Design of Structural Sandwich Panels, Pergamon Press, Oxford, England, 1969
- [2] Vinson, J. R., The Behavior of Sandwich Structures of Isotropic and Composite Materials, Technomic Publishing, Lancaster, USA 1999
- [3] Reddy, J. R., Mechanics of Laminated Composite Plates, CRC Press, Boca Raton, USA, 1996
- [4] Hohe, J., Becker, W., Effective Stress-Strain Relations for Two-Dimensional Cellular Sandwich Cores: Homogenization, Material Models and Properties, Appl Mech Rev, Vol. 55, No. 1, pp. 61-87, 2002
- [5] Scarpa, F., Blain, S., Lew, T., Perrott, D., Ruzzene, Yates, J. R., Elastic Buckling of Hexagonal Chiral Cell Honeycombs, Composites, Part A, 2006, In Press
- [6] Dugundji, J., Cantilever Boundary Condition, Deflections, and Stresses of Sandwich Beams, AIAA Journal, Vol. 40, No. 5, May 2002, pp. 987-995
- [7] Petras, A., Sutcliffe, M. P. F., Failure Mode Maps for Honeycomb Sandwich Panels, Composite Structures, Vol. 44, 1999, pp. 237-252
- [8] Mohr, D. Multi-Scale Finite-Strain Plasticity Model for Stable Metallic Honeycombs Incorporating Microstructural Evolution, Int. Journal of Plasticity, Vol. 22, 2006, pp. 1899-1923
- [9] Daniel, I. M., Abot, J. L., Fabrication, Testing and Analysis of Composite Sandwich Beams, Composites Science and Technology, Vol. 60, 2000, pp. 2455-2463
- [10] Chuang, C.-H., Huang, J.-S., Effects of Solid Distribution on the Elastic Buckling of Honeycombs, Int. Journal of Mechanical Sciences, Vol. 44, 2002, pp. 1429-1443
- [11] Li, K., Gao, X.-L., Subhas, G., Effects of Cell Shape and Cell Wall Thickness Variations on the Elastic Properties of Two-Dimensional Cellular Solids, Int. Journal of Solids and Structures, Vol. 42, 2005, pp. 1777-1795
- [12] Zhang, J., Ashby, M. F., The Out-Of-Plane Properties of Honeycombs, Int. Journal of Mechanical Sciences, Vol. 34, No. 6, 1992, pp.475-489
- [13] McDowell, D. L., Wang, A.-J., Yield Surfaces of Various Periodic Metal Honeycomb at Intermediate Relative Density, Int. Journal of Plasticity, Vol. 21, 2005, pp. 285-320
- [14] Ford, C. M., Gibson, L., J., Uniaxial Strength Asymmetry in Cellular Materials: An Analytical Model, Int. Journal of Mechanical Sciences, Vol. 40, No. 6, pp., 521-531, 1998
- [15] Burton, W. S., Noor, K. A., Assessment of Computational Models for Sandwich Panels and Shells, Computational Methods in Applied Engineering, Vol. 124, 1995, pp. 125-151
- [16] Huang, J. S., Liu, S. Y., Fatigue of Honeycombs Under In-Plane Multiaxial Loads, Materials Science and Engineering, A308, 2001, pp. 45-52



- [17] Demelio, G, Genovese, K., Pappalettere, C., Experimental Investigation of Static and Fatigue Behaviour of Sandwich Composite Panels Joined By Fasteners, Composites, Part B, 2001, pp. 299-308
- [18] Cunningham, P. R., White, R. G., Aglietti, G. S., The Effects of Various Parameters on the Free Vibration of Doubly Curved Composite Sandwich Panels, Journal of Sound and Vibration, 2000, Vol. 230 No. 3, pp. 617-648
- [19] Qiu, X., Deshpande, V.S., Fleck, N.A., Impulsive Loading of Clamped Monolithic and Sandwich Beams Over a Central Punch, Journal of the Mechanics and Physics of Solids, Vol. 53, 2005, pp. 1015-1046
- [20] Saito, t, Parbery, R. D., Okuno, S., Kawano, S., Parameter Identification for Aluminum Honeycomb Sandwich Panels Based on Orthotropic Timoshenko Beam Theory, Journal of Sound and Vibration, Vol. 208, No. 2 , 1997, pp. 271-287
- [21] Seepersad, C. C., Dempsey, B., M., Allen, J. K., Mistree, F., McDowell, D. L., Design of Multifunctional Honeycomb Materials, 9<sup>th</sup> AIAA/ISSM Symposium on Multidiciplinary Analysis and Optimization, Atlanta Georgia, 2002
- [22] Kalamkarov, A. L., Saha, G. C., Georigades, A. V., General Micromechanical Modeling of Smart Composite Shells With Application to Smart Honeycomb Sandwich Structures, Composite Structures, 2005, In Press
- [23] Hohe, J., A Direct Homogenization Approach for Determination of the Stiffness Matrix for Microheterogeneous Plates with Application to Sandwich Panels, Composites, Part B, Vol. 34, 2003, 615-626
- [24] Glenn, C. E., Hyer, M. W., Bending Behavior of Low-Cost Sandwich Plates, Composites: Part A, Vol. 36, 2005, pp. 1449-1465
- [25] Xu, X. F., Qiao, P., Homogenized Elastic Properties of Honeycomb Sandwich With Skin Effect, Int. Journal of Solids and Structures, Vol. 39, 2002, pp. 2153-2188
- [26] Davalos, J. F., Qiao, P., Xu, X. F., Robinson, J., Barth, K. E., Modeling and Characterization of Fiber Reinforced Plastic Honeycomb Sandwich Panels for Highway Bridge Applications, Composite Structures, Vol. 52, 2001, pp. 441-452
- [27] Hohe, J., Becker, W., A Refined Analysis of the Effective Elasticity Tensor for General Cellular Sandwich Cores, Int. Journal of Solids and Structures, Vol. 38, 2001, pp. 3689-3717
- [28] Paik, J., K., Thayamballi, A. K., Kim, G. S., The Strength Characteristics of Aluminum Honeycomb Sandwich Panels, Thin Walled Structures, Vol. 35, 1999, pp. 205-231
- [29] Santoza, S., Wiezbicki, T., Effect of an Ultralight Metal Fiber on the Bending Collapse Behavior of Thin-Walled Prismatic Columns, Int. Journal of Mechanical Sciences, Vol. 41, 1999, pp. 995-1019
- [30] Hayes, A. M., Wang, A., Dempsey, B. M., Mcdowell, D. L., Mechanics of Linear Cellular Alloys, Mechanics of Materials, Vol. 36, 2004, pp. 691-713
- [31] Myers, D. E., Martin, C. J., Blosser, M. L., Parametric Weight Comparison of Advanced Metallic, Ceramic Tile, and Ceramic Blanket Thermal Protection Systems, NASA/TM-200-210289
- [32] Ko, W. L., Heat Shielding Characteristics and Thermostructural Performance of a Superalloy Honeycomb Sandwich Thermal Protection System (TPS), NASA TP, 2004, NASA/TP-2004-212024

- [33] Lampani, L., Keller, K., Pfeiffer, E., Ritter, H., Gaudenzi, P., Variable Curvature Concepts for Smart Thermal Protection Systems (Smart TPS), IAC-05-C2.4.01,
- [34] Gibson, L. J., Modeling the Mechanical Behavior of Cellular Materials, Materials Science and Engineering, Vol. A110, 1989, 1-36
- [35] Meraghni, F., Desrumaux, F., Benzeggagh, M. L., Mechanical Behaviour of Cellular Core for Structural Sandwich Panels, Composites, Part A, 1999, pp. 767-779
- [36] Kim, H. S., Al-Hassani, S. T. S., A Morphological Elastic Model of General Hexagonal Columnar Structures, Int. Journal of Mechanical Sciences, Vol. 43, 2001, pp. 1027-1060
- [37] Wicks, N., Hutchinson, J. W., Optimal Truss Plates, Int. Journal of Solids and Structures, Vol. 38, 2001, pp. 5165-5183
- [38] Rathburn, H. J., Zok, F. W., Evans, A. G., Strength Optimization of Metallic Sandwich Panels Subject to Bending, Int. Journal of Solids and Structures, Vol. 42, 2005, pp. 6643-6661